Increasing the hot-corrosion resistance of thermal barrier coating systems by the addition of oxides of Cr and Mg

by

Joseph Paul Schramm

A thesis submitted to the graduate faculty
in partial fulfillment of the requirements for the degree of
MASTER OF SCIENCE

Major: Materials Science and Engineering

Program of Study Committee:
Daniel Sordelet, Co-major Professor
Brian Gleeson, Co-major Professor
Palaniappa Molian
Ralph Napolitano

Iowa State University
Ames, Iowa
2003

Graduate College

Iowa State University

This is to certify that the master's thesis of

Joseph Paul Schramm

has met the thesis requirements of Iowa State University

Signatures have been redacted for privacy

Table of Contents

Acknowledgements

I would like to thank my family for their unconditional support in everything I've done. I would like to thank my major professors, Dan Sordelet and Brian Gleeson, for their advice, insight and opinions, in addition to their general good nature. I would like to thank Matt Besser, who prepared all of my coated samples, for technical support and enjoyable conversation. I would also like to thank Matt and Dan for giving me a job and getting me interested and involved in research four years ago. I would like to thank my officemates: Shigenari Hayashi, Vinay Deodeshmukh, Bingtao Li, and Wen Wang for alternative views on confusing experimental results and other general discussion. I would also like to thank Norm Bornstein for his role as a consultant on this project.

The work presented in this thesis was funded by the Office of Naval Research under contract N00014-00-1-0008.

Abstract

The present research seeks a simple, economical method to improve the hot corrosion resistance of the substrate/TBC system by modifying the top-coat of the TBC. The yttria-stabilized zirconia (YSZ) top coat was deposited via air plasma spraying and the top coat modification methods investigated involved (1) infiltration with aqueous solutions of water-soluble compounds of chromium (*e.g.*, chlorides, nitrates, acetates) and alkaline earth elements (*e.g.*, $MgCrO_4 \cdot xH_2O$) followed by an oxidizing conversion treatment and (2) co-depositing Cr_2O_3 with the YSZ. The goal of these modifications was to deliver alkaline earth and/or chromium oxides for reaction with the molten salt, thereby inhibiting its penetration through the top-coat and/or its reactivity with the substrate alloy. Hot corrosion testing included pre-deposited salt film, Dean Rig, and crucible tests with either Na_2SO_4 or Na_2SO_4-$CaSO_4$-$MgSO_4$ eutectic as the corrosive salt. It was found that the coating modifications could have a favorable effect on the chemistry of the salt and the hot-corrosion resistance of the TBC system. It was further found that the corrosiveness of a given salt was very dependent on the type of test conducted, *i.e.*, thin-film pre-deposit of the salt onto the sample or submersion of the sample into molten salt.

Chapter 1: Introduction

The phenomenon of hot corrosion has been observed in gas turbine engines since the mid-1950s (1), and has been the topic of significant research since the 1960s. Hot corrosion is an accelerated attack of a metal in the presence of a film of liquid salt. This accelerated attack can occur on blades and vanes in gas turbine engines and greatly reduce the life of these engine parts. Hot corrosion is known to occur at temperatures as low as 650°C and roughly as high as 1000°C. In gas turbine engines, it is common practice to coat the blades and vanes with a thermal barrier coating (TBC) which allows the engine to run at a higher temperature, and therefore, more efficiently. The TBC consists of an oxidation resistant bond-coat, most commonly a plasma sprayed MCrAlY (where *M* is Ni, Co or a combination of the two) or diffusion-type aluminide, upon which an oxide is thermally grown, and a top-coat made of yttria-stabilized zirconia (YSZ). The top-coat is formed by either air plasma spraying (APS) or electron-beam plasma-vapor deposition (EB-PVD). These two coating methods enhance strain tolerance and decrease thermal conductivity of YSZ by producing pores and microcracks in its microstructure. However, these pores provide a pathway for molten salt to access the underlying metallic bond coat and substrate. When molten salt penetrates through the network of pores, it has the ability to dissolve the protective oxide layer of the metal, thus decreasing the adhesion of the TBC and allowing the accelerated attack of the metal.

Many advancements have been made in the strength, oxidation resistance and hot corrosion resistance of metals used in gas turbine engines, but very little has been done with the ceramic portions of thermal barrier coatings. The work presented in this thesis is concerned with increasing the hot

corrosion resistance of gas turbine engine parts by modifying the chemistry of the ceramic portion of the thermal barrier coating. The goal of these coating modifications is to supply elements that have the ability to change the chemistry and/or phase composition of the molten salt associated with hot corrosion attack so as to reduce the activeness of the salt in causing accelerated attack.

This thesis covers the production of modified thermal barrier coating samples, the hot corrosion testing of these samples, and several experiments concerning the conditions under which hot corrosion tests take place, and is organized as follows:

- Chapter 2 is an brief introduction to gas turbine engines and the materials used in the production of the blades and vanes of gas turbines.
- Chapter 3 is a survey of the literature with respect to the mechanisms of and the conditions associated with hot corrosion in gas turbine engines.
- Chapter 4 is a discussion of the procedures used in the preparation of thermal barrier coating samples and hot corrosion experiments.
- Chapter 5 includes the results of the experiments described in Chapter 4.
- Chapters 6 and 7 cover a summary of this thesis and suggested future work, respectively.

Chapter 2: Gas Turbine Engines

The general features of the gas turbine engine are shown in Figure 1. Air is taken in through the nozzle of the engine and is compressed by the various compressor regions. In addition to increasing the pressure of the air, this compression preheats the air before it enters the combustion chamber. Combustion serves to heat the air further increasing the pressure just before it enters the turbine section of the engine. The turbine rotors are connected, via an axial shaft, to some or all of the compressor rotors, so as the hot, high-pressure gas is forced through the turbine, it assists in the compression of fresh air entering the compressor. Because the gas turbine is a heat engine, the efficiency of is related to the maximum and minimum temperatures in the cycle. One way of increasing efficiency is to increase the temperature at the entry of the turbine. This temperature has increased from 700°C in the gas turbines of the 1940's to roughly 1350°C in modern gas turbines(1). The increasing operating temperatures of turbines have been made possible by advances in the metals (superalloys) used in the construction of turbines and ceramic thermal barrier coating (TBC) systems.

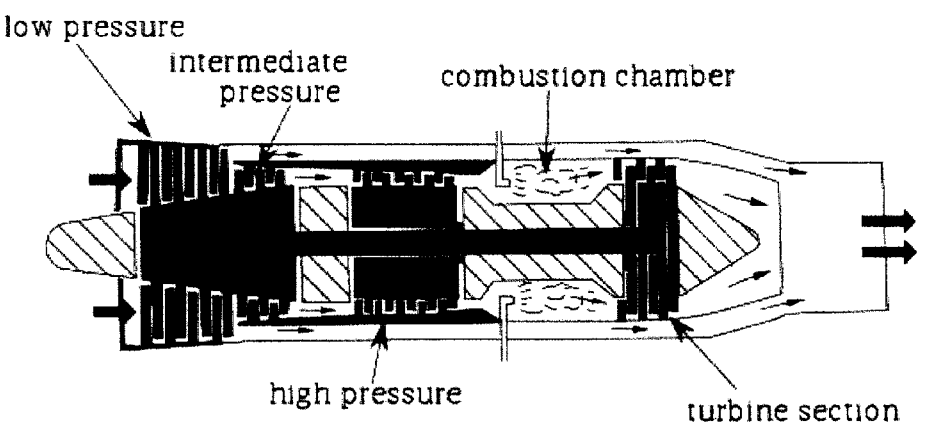

Figure 1. Schematic diagram of axial-flow gas turbine engine with by-pass duct (After (2))

2.1 Superalloys in Gas-Turbine Applications

Superalloys are nickel-, iron-nickel-, and cobalt-based alloys made for use at elevated temperatures. They usually are face centered cubic (FCC) in crystal structure, and are made to have high-temperature strength, corrosion and oxidation resistance, or both. Superalloys are used as the blades and vanes in the compressors and turbines of gas turbine engines. Nickel is a noteworthy base metal in that it has solubility for a number of metals. This allows for a wide variety of commercially available alloys with a wide variety of properties, high temperature strength and corrosion resistance being the most important properties.

The strength of nickel-base alloys mainly comes from one or a combination of three different sources: solid solution strengthening, carbide strengthening, and precipitation hardening. Solid solution strengthening is achieved by adding elements that differ only slightly in atomic diameter from Ni (*e.g.* Co, Fe, Cr, Mo, W, V, Ti, Al). These elements, when in solid solution with Ni cause a local change in the lattice that confers hardening to the alloy. Carbide strengthening occurs when elements alloyed with Ni form carbides. Several different metal carbide stoichiometries (*e.g.* MC, M_6C, M_7C_3, $M_{23}C_6$) can be formed, and, generally speaking, those with more metal atoms per unit cell (M_7C_3 and $M_{23}C_6$) are more favorable, but only in cases where they are well dispersed. Agglomeration of carbides can cause embrittlement. The third method of strengthening Ni-base alloys is the precipitation of γ'-Ni_3(Al, Ti). This intermetallic phase is unique in that it has an ordered FCC structure that has a nearly identical lattice constant to the γ matrix, which results in low interfacial energy and long-time stability in addition to considerable strengthening of the alloy.

Corrosion and oxidation resistance of Ni-base alloys comes primarily from the addition of Cr and Al, as they assist in the formation of protective oxide layers(3). As seen in Figure 2, the use of Cr as an alloying agent increases the resistance of an alloy to oxidation and corrosion(4).

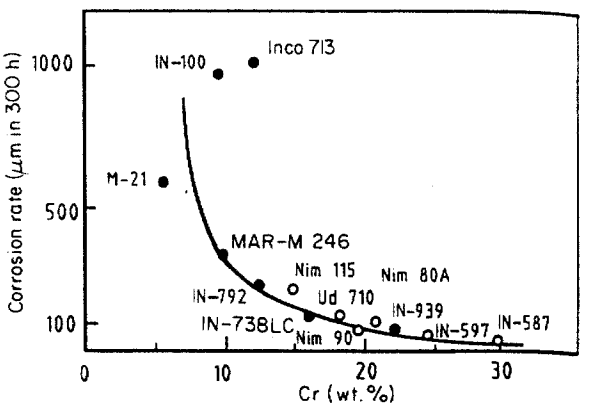

Figure 2. Oxidation rate as a function of wt.% Cr (taken from Hancock (4)).

The two metal substrate materials used in the present study are nickel 200 and Haynes 214. Nickel 200 is a commercially pure nickel, and Haynes 214 is a nickel-chromium-aluminum-iron wrought alloy designed for high-temperature oxidation resistance (above 955°C, 214 forms a pure Al_2O_3 scale)(5). The compositions of these alloys are shown in Table 1(3).

Table 1. Compositions of metals investigated in this study (from(3)).

	Composition[a], wt%											
Alloy	Ni	Cr	Al	Fe	C	Cu	Mn	Si	S	Co	Mo	Other
Nickel 200	99.0[b]	---	---	0.40	0.15	0.25	0.35	0.35	0.01	---	---	---
Haynes 214[c]	bal	16.0	4.5	3.0	0.05	---	0.5	0.2	---	2.0	0.5	0.5 W 0.5 Ti 0.0006 B 0.05 Zr 0.002-0.040 Y

a Maximum value except where noted
b Minimum value
c Nominal composition

Nickel 200 was chosen because of the relative simplicity of its chemistry and its poor resistance to hot corrosion. Pure nickel has also been the subject of much hot corrosion research(6-9). Haynes 214 was chosen for its Al_2O_3-forming characteristics and its chemical similarity to the typical MCrAlY bond-coat.

2.2 Thermal Barrier Coatings

The ability of gas turbine engines to run at temperatures above the melting point of most superalloys has been made possible by the use of ceramic thermal barrier coatings (TBCs). A typical TBC system, schematically represented in Figure 3, consists of an oxidation resistant bond-coat (~100μm), most commonly an MCrAlY (where *M* is Ni, Co or a combination of the two) or aluminide coating, a thermally grown oxide (1-10μm), and a top-coat (100-400μm) typically composed of yttria-stabilized zirconia (YSZ).

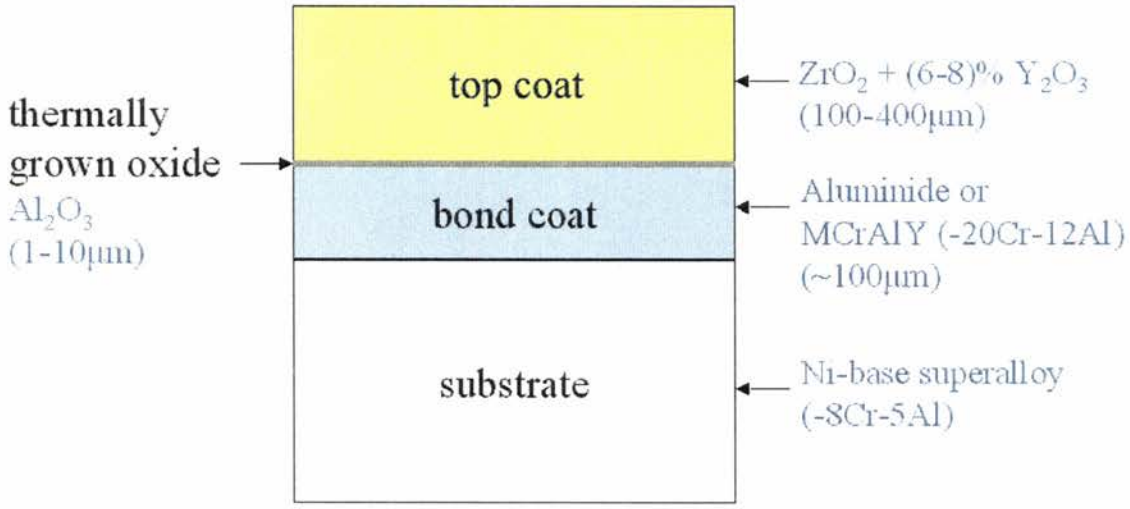

Figure 3. Structure and materials of a typical thermal barrier coating.

In the deposition of a TBC system, the bond-coat is usually either plasma sprayed at low pressure (LPPS) for MCrAlY coatings or diffusion formed by a vapor process in the case of aluminide coatings, then an oxide is thermally grown upon the bond-coat. Finally, the top-coat is formed by either air plasma spraying (APS) or electron-beam physical vapor deposition (EB-PVD).

In order to function in a gas turbine engine, the top-coat must have low thermal conductivity, a coefficient of thermal expansion (CTE) comparable to that of the base metal, and a fair amount of strain tolerance to resist fracture under the stresses that occur in the blade of a gas turbine. YSZ has a low thermal conductivity (~2.3 $W \cdot m^{-1} K^{-1}$ at 1000°C for a fully dense sample(10)) and a relatively high coefficient of thermal expansion (~11×10^{-6} K^{-1}). YSZ also has excellent abrasion resistance due to its high hardness. At low temperatures, pure ZrO_2 is thermodynamically stable in the mechanically unsound monoclinic crystal structure. Yttria is added to zirconia to stabilize the mechanically sound tetragonal crystal structure. The introduction of microcracks and pores from the APS and EB-PVD processes gives the top-coat a degree of strain tolerance to withstand the stresses and strains induced in a gas turbine system. With APS coatings, the microcracks are perpendicular to the direction of heat flow and thus, make the material more thermally insulating(11).

2.2.1 Air Plasma Spraying

Air Plasma Spraying has been utilized as the YSZ top-coat deposition method in this study. APS is a thermal spray method in which an electric arc creates a plasma that can reach temperatures of more than 16000°C

(12). The material to be sprayed is injected into the plasma arc as a powder where it is fully melted and propelled toward the substrate by the plasma arc gas. The molten particles impact against the substrate and are rapidly solidified forming a continuous, but typically porous, coating. A diagram of a typical plasma arc gun is shown in Figure 4.

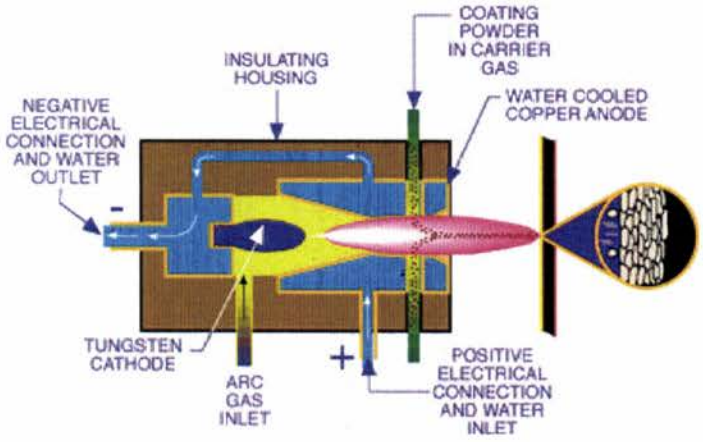

Figure 4. Diagram of a typical plasma arc gun used in the APS process.

The high temperature of the plasma allows the spraying of practically any material and the injection of materials as powder creates the opportunity to spray coatings with tailored compositions and microstructures. The substrates used in plasma spraying are prepared by several cleaning steps and grit-blasting to roughen the surface for increased coating adherence. The APS method is commonly used in the production of TBC layers because it is easy to develop the porosity that gives the ceramic coating a high degree of toughness, or strain tolerance, which, as noted above, is a necessity in gas turbine engine systems. In addition, the porosity in the APS coating acts in a beneficial manner to decrease its thermal conductivity.

2.2.2 TBC Degradation and Failure

This study is not particularly concerned with assessing the wide variety of failure mechanisms in TBC systems. Rather, the focus here is on the damage to the interfaces between the top-coat, TGO, and bond-coat that creates pathways for molten salt to come into direct contact with the metal in the bond-coat. This failure mechanism is a variant of hot corrosion within TBC systems and has several causes including thermal cycling, differences in thermal expansion coefficient at both the top-coat/TGO and TGO/bond-coat interfaces, and the continuous constrained growth of the TGO at operating temperatures. In addition to causing failure at the interfaces, these factors can cause additional cracking of the ceramic top-coat which generates enlarged pathways for salt access. When a molten salt is brought into the system and infiltrates the pores of an APS coating, differential volume changes can also cause fracture of the top-coat. It is important to consider these factors in the evaluation of a TBC system operating under conditions that favor hot corrosion.

Chapter 3: Background on Hot Corrosion

3.1 Introduction

Hot corrosion is, in general terms, the accelerated attack of materials caused by the presence of a salt deposit(13). The more restrictive definition used in this thesis is that hot corrosion is the accelerated oxidation of metals caused by the presence of a liquid salt deposit. Hot corrosion attack can be divided as being either Type I, termed sulfidation by DeCrescente and Bornstein(14), or Type II. This division depends on the temperature range at which the corrosion process occurs, as shown schematically in Figure 5.

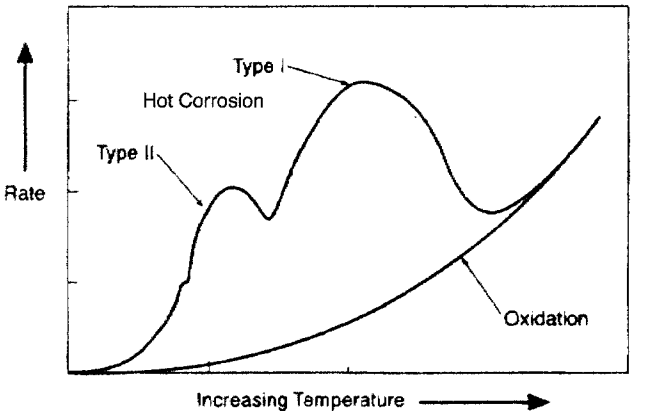

Figure 5. Temperature dependence of rate of hot corrosion and oxidation attack (taken from Bornstein(15)).

Figure 5 shows a general relationship between temperature and the rate of hot corrosion and oxidation attack (15). Two maxima can be seen in the curve for hot corrosion distinguishing the two types of attack by temperature range. Generally, the metallographic appearance of the

corrosion is used to differentiate the two types. Type I hot corrosion occurs at higher temperatures (above 800°C), and is characterized by a broad corrosion front and internal sulfides rich in Cr coupled with a zone depleted in reactive elements like Cr, Al, and Ti (1). An example of the broad front of corrosion exhibited by Type I hot corrosion is shown in Figure 6. Note the porous, nonprotective oxide and light gray sulfides in the alloy. Type I hot corrosion also shows a depletion zone in the alloy, which stretches into the alloy to the point of the deepest sulfide precipitation.

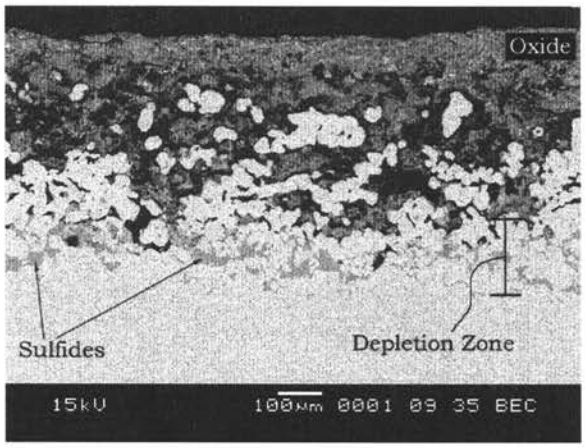

Figure 6. Haynes 214 showing Type I hot corrosion in the presence of Na_2SO_4.

Type II hot corrosion occurs at lower temperatures (roughly 650°C to 775°C) (15), and is characterized by a localized pitting attack. Neither internal sulfides nor an alloy depletion zone are characteristic of Type II hot corrosion (1). This type of hot corrosion is not expected to be observed in this study, as all testing is taking place at 900°C, well above the temperature regime where Type II behavior tends to dominate.

In addition to high temperature, a molten salt is needed to create hot corrosion conditions. It is important to understand the nature (*i.e.*, composition and chemistry) of this salt to understand the nature of the

accelerated hot corrosion attack. Simons *et al.* (16) observed that two types of deposits were formed at the same temperature on the first-stage nozzle of a gas turbine aeroengine, a powdery deposit and a dense deposit, both consisting primarily $CaSO_4$ and Na_2SO_4. It was found that the dense (previously molten) deposits contained higher amounts of Na_2SO_4 than the powdery ones. From this and the phase diagram for the Na_2SO_4-$CaSO_4$ system (Figure 7) the importance of Na_2SO_4 in the melting of salt deposits can be confirmed. The ability of Na_2SO_4 to cause hot corrosion was confirmed by crucible tests of type 310 steel in which a piece of the steel was submerged in molten Na_2SO_4(16).

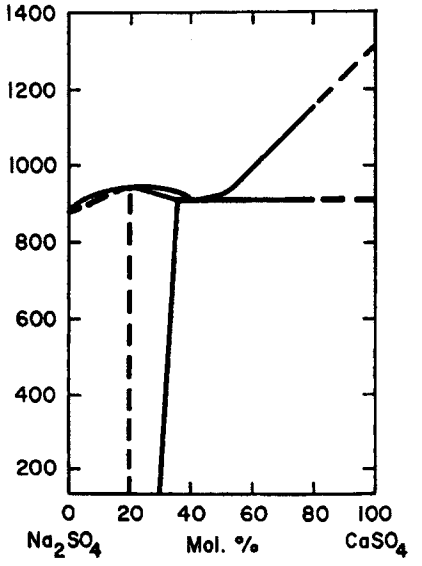

Figure 7. Phase diagram of Na_2SO_4-$CaSO_4$ system (from (17))

Na_2SO_4 is only a minor constituent of sea salt, and not found commonly in air, so understanding the mechanism of its formation in a gas turbine atmosphere is important. NaCl, from sea salt, is commonly observed in the surroundings, either as an aerosol or from seawater contaminating fuel transported by ship(15). Dew point calculations (14) have shown that,

under gas turbine conditions, NaCl is stable as a vapor, not a condensed phase, so it is not deposited on turbine components. Sulfur is a common impurity in jet fuel, and, during combustion, is converted to sulfur oxides, SO_2 and SO_3. These sulfur oxides react with the NaCl vapor according to equations 1 and 2 to form condensed Na_2SO_4(14). The Helmholtz free energy changes for these reactions were calculated from standard state free energies of formation.

$$2NaCl + SO_2 + \tfrac{1}{2}O_2 + H_2O = Na_2SO_4 + 2HCl$$
$$\Delta F(1200K) = -41.37\,\text{kcal/mol} \qquad (1)$$

$$2NaCl + SO_3 + H_2O = Na_2SO_4 + 2HCl$$
$$\Delta F(1200K) = -44.59\,\text{kcal/mol} \qquad (2)$$

Calculations showed that at 1000°C and atmospheric pressure, the conversion of NaCl to Na_2SO_4 and HCl should go to 75% completion, and at common gas turbine operating conditions (much higher pressures and possibly lower temperatures at the alloy surface) the reaction is assumed to go to complete conversion(14). This was confirmed by a burner-rig test, as will be described in Chapter 4. The chemistry of the salt deposited on the burner rig specimens was quantitatively analyzed, and the $Na^+ : SO_4^{2-}$ ratio was found to be approximately 2, with Cl^- concentrations nearly three orders of magnitude less than Na^+. This work established that when sodium is present in a gas turbine atmosphere, it is primarily in the form of a sulfate, not a chloride.

The ability of certain atmospheres to form sulfides of the reactive alloying elements (Cr and Al) can be determined by calculating the sulfur potential,

Ps_2, for several atmospheres and the sulfides of Cr and Al (*i.e.*, their dissociation pressures). In order to form sulfides of Cr and/or Al, Ps_2 must be higher for the atmosphere than for the sulfides. DeCrescente and Bornstein (14) found that at 900°C, liquid Na_2SO_4 and pure SO_2 can cause sulfide formation, but neither an equilibrium Na_2SO_4/O_2 vapor mixture at 900°C nor a dilute SO_3/O_2 mixture have high enough Ps_2. These calculations were also verified experimentally(14). As the atmosphere of a gas turbine engine is generally a mixture of O_2, SO_2, and SO_3, the sulfides found in an alloy after exposure to this type of an atmosphere were almost certainly formed in the presence of a liquid salt.

3.2 Mechanisms of Type I Hot Corrosion

Two well-known mechanisms of Type I hot corrosion will be discussed here. The first is the oxide fluxing mechanism proposed by Goebel and Pettit (6, 18). This mechanism takes a thermochemical approach to describe the fluxing of the metal oxide scale and the formation of metal sulfide. The second mechanism takes an electrochemical approach, and is based on measurements of the solubilities of oxides in fused Na_2SO_4, carried out by Rapp *et al.* (7, 8, 19-22).

3.2.1 Fluxing

Goebel and Pettit (6) proposed a fluxing mechanism for hot corrosion of pure Ni. They inferred that since the oxygen and sulfur activities in the vapor and condensed phases of Na_2SO_4 must be the same and that the condensed phase is required for accelerated corrosion (as proven by DeCrescente and Bornstein(14)), then a composition gradient must be established across the

Na_2SO_4 layer. From phase stability diagrams and an estimate of the oxygen and sulfur activities in a gas turbine atmosphere, it can be determined that NiO can form and that there would be a consequential depletion of oxygen near the Na_2SO_4/NiO interface. The oxygen can come from the decomposition of Na_2SO_4 (as O^{2-} or O_2) by equations 3-5 or from the surrounding atmosphere (as dissolved O_2).

$$Na_2SO_4 = Na_2O + SO_3 \quad (3)$$

$$Na_2O = 2Na^+ + O^{2-} \quad (4)$$

$$SO_3 = \tfrac{1}{2}S_2 + \tfrac{3}{2}O_2 \quad (5)$$

From equations 3 and 5 it is seen that an increase in O_2 or O^{2-} activity necessarily means a decrease in sulfur activity, and vice versa. As the oxygen concentration and activity are decreased by the oxidation of Ni, there should be marked increase in the sulfur activity in the Na_2SO_4 (6). This increased sulfur activity can be high enough to lead to the eventual formation of nickel sulfide beneath the oxide scale. This sulfide formation would cause a local decrease in sulfur activity and create favorable conditions (high oxide ion activity) for the fluxing of the NiO scale by equation 6 or 7(6). The mechanism by which the sulfur penetrates the NiO scale is not well understood.

$$NiO + O^{2-} = NiO_2^{2-} \quad (6)$$

$$2NiO + O^{2-} + \tfrac{1}{2}O_2 = 2NiO_2^- \quad (7)$$

Nickelate ions then diffuse away from the NiO/Na_2SO_4 interface to a point where the O^{2-} activity is low enough that NiO_2^{2-} precipitates as NiO. This precipitation creates a discontinuous, nonprotective oxide at the Na_2SO_4/gas interface, which allows the salt to come into contact with the alloy, and accelerated oxidation is maintained until the Na_2SO_4 can no longer flux the NiO (6). Figure 8 summarizes Goebel and Pettit's fluxing model for the Na_2SO_4-induced accelerated oxidation of nickel (6).

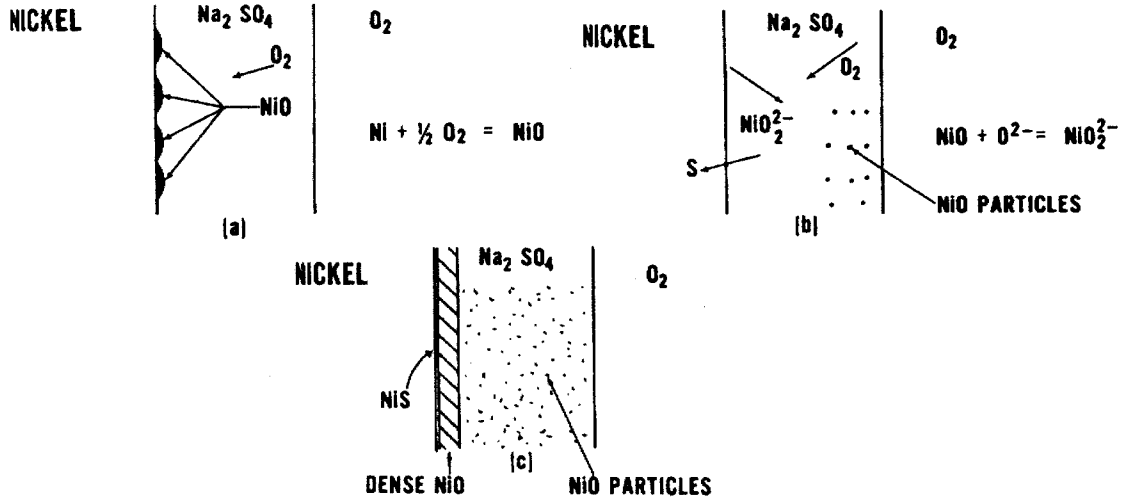

Figure 8. Model for Na_2SO_4-induced accelerated oxidation of pure nickel. (a) Oxygen activity gradient is produced by initial oxidation of nickel. (b) Sulfur enters alloy and oxygen ions react with NiO to form nickelate ions. (c) Sulfur no longer enters the alloy, oxide ions are no longer produced, Na_2SO_4 becomes saturated with Ni, and a continuous NiO scale is formed. (after Goebel and Pettit (6)).

Goebel, Pettit, and Goward (18) expanded this proposed mechanism by considering several nickel-base alloys. Of particular interest to this thesis are those containing Cr and Al. The authors observed that Ni-1wt.% Al underwent hot corrosion attack much like pure Ni, but for Ni-31wt.% Al, accelerated oxidation only occurred only for samples coated with a large amount of salt. The accelerated oxidation in Ni-31Al was observed after an

incubation period, during which, weight gain was similar to oxidation without Na_2SO_4. Aluminum sulfides were observed in the alloy indicating that the sample underwent Type I accelerated attack.

In Ni-Cr alloys, containing as little as 5 wt.% Cr, accelerated attack was not observed. This was ascribed to the fact that during the initial stages of oxidation, CrO_4^{2-} forms immediately from Cr_2O_3 creating an environment where Cr_2O_3 is relatively stable as a protective layer on the surface of the alloy. An example of this reaction is represented in equation 8.

$$Cr_2O_3 + \tfrac{3}{2}O_2 + 2SO_4^{2-} = 2CrO_4^{2-} + 2SO_3 \qquad (8)$$

This results in a reduction of the oxide ion concentration at the Na_2SO_4/Cr_2O_3 interface (*i.e.*, due to an increase in SO_3) so that the remaining oxide (NiO, Al_2O_3, Cr_2O_3) is stable in the salt, and the onset of accelerated oxidation is significantly delayed.

An Al_2O_3 scale is subject to the same type of fluxing mechanism as Cr_2O_3, except that the reaction does not involve dissolved O_2, as shown in equation 9.

$$Al_2O_3 + SO_4^{2-} = 2AlO_2^- + SO_3 \qquad (9)$$

This also results in a reduction of the oxide ion concentration, making Al_2O_3 stable. If the salt layer is thick, it can dissolve a higher amount of Al_2O_3 before reaching the equilibrium concentration of AlO_2^- in the salt. This means that it will be easier (via grain boundaries and a thinner oxide layer) for the salt to access the metal through the oxide scale.

An alloy containing Al and Cr can be quite resistant to hot corrosion because Cr_2O_3 dissolves faster than Al_2O_3, to the extent that the Al_2O_3 becomes somewhat stabilized. Any sulfur that gains access to the metal will form Cr-rich sulfides instead of Al-rich sulfides. This allows the Al_2O_3 to remain stable on the alloy, and results in a lower rate of oxidation since Al-rich sulfides are nonprotective(18).

3.2.2 Oxide Solubility

According to Rapp and Goto(23), the solubility of metal oxides in fused Na_2SO_4 and the solubility gradient across the salt can be used to determine whether an alloy will undergo sustained or limited hot corrosion attack. The solubility of an oxide in Na_2SO_4 changes as a function of the acidity of the Na_2SO_4. The acid-base chemistry of Na_2SO_4 can be described in a manner similar to that of aqueous solutions (24):

$$\begin{aligned} &Na_2O + SO_{3(g)} = Na_2SO_4 \\ &\log K(1200K) = -16.7 \end{aligned} \qquad (10)$$

so for pure Na_2SO_4:

$$\log a_{Na_2O} + \log a_{SO_3} = -16.7 \qquad (11)$$

The acidity of the molten salt can be expressed as $\log a_{SO_3}$ and the basicity as $\log a_{Na_2O}$. This convention makes it straightforward to construct an oxide solubility plot, *e.g.* Figure 9. The condition required for sustained hot corrosion attack, introduced by Rapp and Goto(23), is described as a "negative solubility gradient." For basic fluxing, as with the mechanism proposed by Goebel and Pettit for pure Ni, this occurs when the oxide has a higher solubility at the oxide/salt interface (I in Figure 9) than at the salt/gas interface (II in Figure 9).

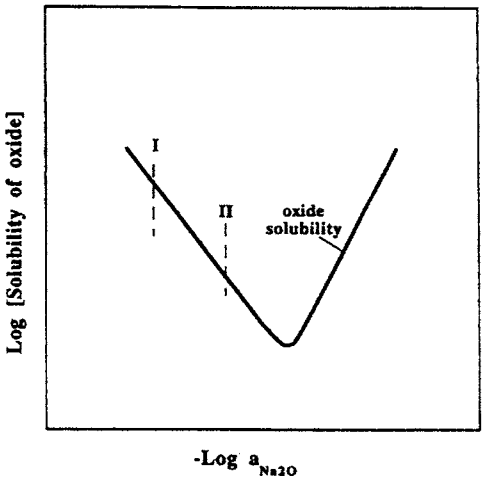

Figure 9. General relation of solubility of oxide in Na_2SO_4 with O^{2-} activity at a constant O_2 partial pressure (after Rapp(24)). For the establishment of a "negative solubility gradient," the conditions at the oxide/salt interface are marked I, and those at the salt/gas interface are marked II.

The solubility of a number of oxides in fused Na_2SO_4 at 1200K (927°C) has been measured. These results, compiled by Rapp(24), are shown in Figure 10. Under the operating conditions of a gas turbine engine, P_{SO_3} values are frequently in the range of the solubility minima of Cr_2O_3 and Al_2O_3 in Na_2SO_4.

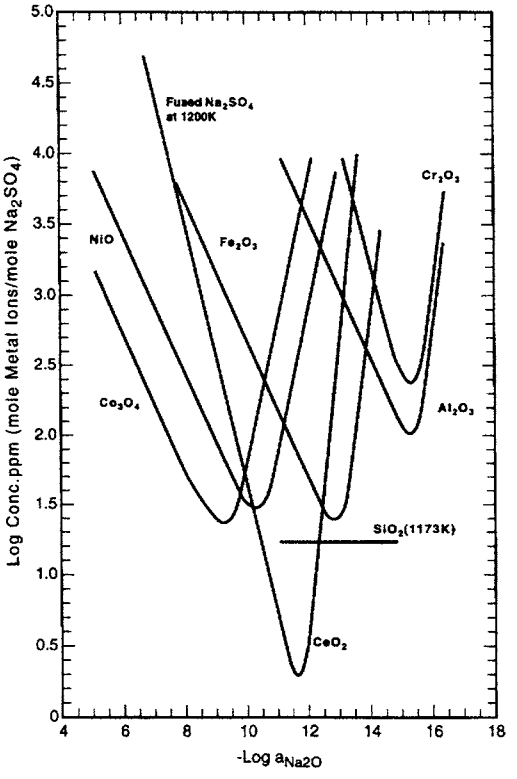

Figure 10. Measured solubilities for several oxides in pure fused Na_2SO_4 (taken from Rapp (24)).

Note that the solubility minimum of NiO occurs at a much higher a_{Na_2O} (*i.e.*, lower –log a_{Na_2O}) than Cr_2O_3 or Al_2O_3. It appears that in a gas turbine atmosphere, NiO would be attacked by acidic fluxing. Otsuka and Rapp (8) measured the basicity and oxygen activity of a thin Na_2SO_4 film on Ni at 900°C. For a short time (~15 minutes), basicity and P_{O_2} remained approximately constant at the equilibrium values set by the atmosphere, then a sharp dip in P_{O_2} and an abrupt increase in basicity occurred as the hot corrosion attack began. The authors concluded that the abrupt increase in basicity was due to the formation of nickel sulfide, by equation 12, as the Na_2SO_4 makes contact with the Ni through grain boundaries or cracks in the protective oxide scale(8).

$$4Ni + Na_2SO_4 = 3NiO + NiS + Na_2O \quad (12)$$

So, despite the acidic conditions in an atmosphere like that of a gas turbine engine, NiO undergoes basic dissolution because of an extreme increase in the local bacisity of the Na_2SO_4 melt.

The presence of a Cr_2O_3 or Al_2O_3 scale precludes the immediate accelerated attack seen with pure Ni because of the formation of a positive solubility gradient. Some specific and simplified examples of this are shown here. Cr_2O_3 and Al_2O_3 are expected to be subjected to a limited amount of basic dissolution in the atmosphere of a gas turbine engine. When the oxidizing species are O_2 and O^{2-}, the basic fluxing reaction for a Cr_2O_3 scale, equation 8, can be written as:

$$Cr_2O_3 + \tfrac{3}{2}O_2 + 2O^{2-} = 2CrO_4^{2-} \quad (13)$$

This reaction results in consumption of dissolved O_2 and an increase in the acidity of the salt (an increase in the amount of dissolved SO_3, Equation 8, or a decrease in the amount of O^{2-} ions in the melt, Equation 13). Two simplified, transient-state cases are described here. In the case of slow diffusion of dissolved O_2 and/or a thick salt layer, the transport of dissolved O_2 limits the reaction. As CrO_4^{2-} is formed, O_2 is consumed at the Na_2SO_4/oxide interface and a P_{O_2} gradient is formed. By Equation 13, the solubility of CrO_4^{2-} at the Na_2SO_4/oxide interface is decreased and a positive solubility gradient is developed, so no fluxing occurs. This situation is shown in Figure 11.

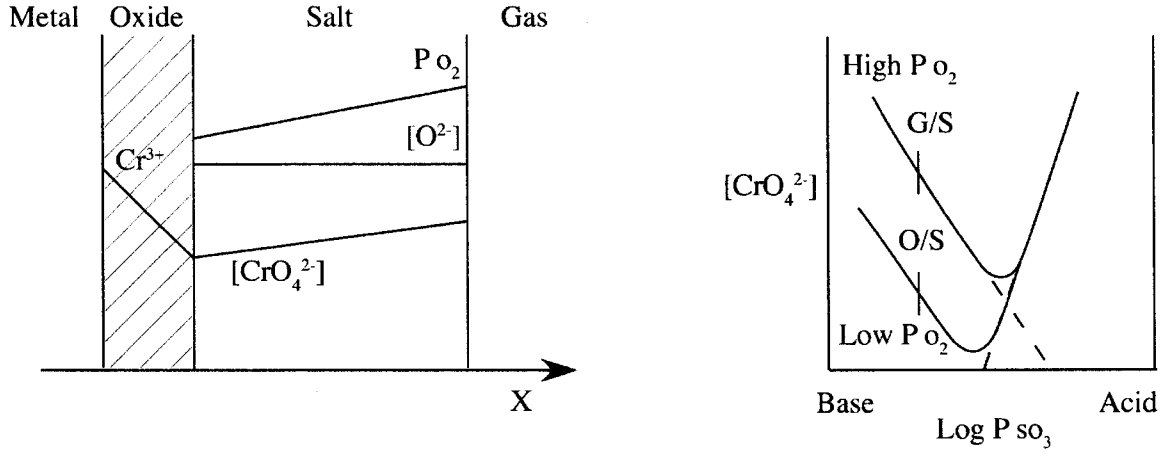

Figure 11. Consumption of O_2 at oxide / salt interface results in lower P_{O_2} and lower oxide solubility at that interface, so no fluxing occurs.

In the case of a thin salt layer and/or fast transport of dissolved O_2, the supply of O^{2-} to the reaction site limits the reaction. The formation of CrO_4^{2-} causes a decrease in $[O^{2-}]$ at the Na_2SO_4/oxide interface and an oxide activity gradient is produced. From Equation 13, a positive solubility gradient is formed and fluxing does not occur. This situation is shown in Figure 12.

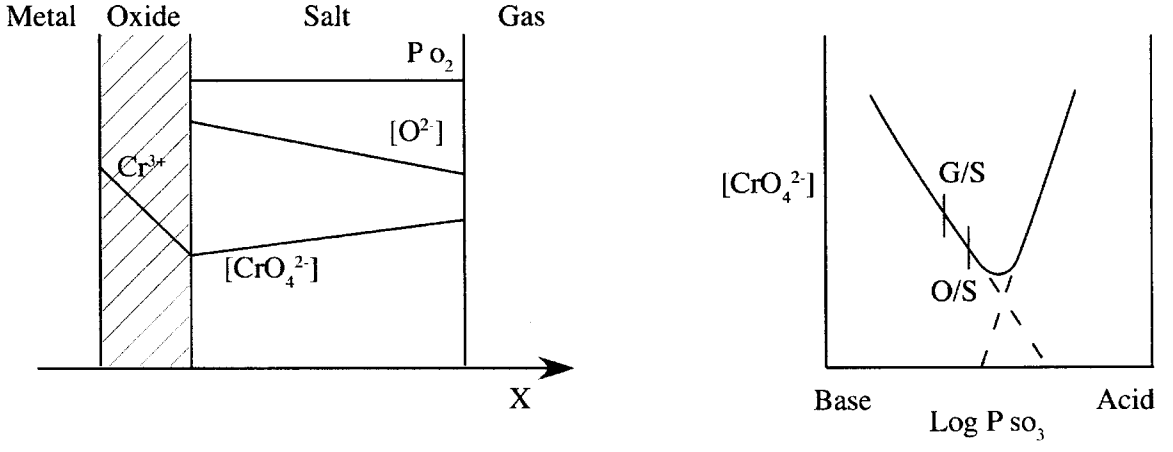

Figure 12. Consumption of O^{2-} increases the acidity at the oxide / salt interface, so a negative solubility gradient is formed, and no fluxing occurs.

The basic dissolution reaction for an Al_2O_3 scale, equation (9), can be rewritten without SO_3.

$$Al_2O_3 + O^{2-} = 2AlO_2^- \qquad (14)$$

This reaction involves only O^{2-} as an oxidant, so dissolved O_2 has no effect on the solubility of Al_2O_3. As the solubility behavior of Al_2O_3 is much like that of Cr_2O_3, the initial stages of oxidation of an Al_2O_3-forming alloy will involve the basic dissolution of Al_2O_3 as AlO_2^-. In a thin salt layer, as with Cr_2O_3 in the transient state shown in Figure 12, a positive solubility gradient is formed, and no fluxing occurs.

Understanding the nature of the solubility of oxides in molten salt is an important step in explaining the fluxing of a protective oxide scale. As seen in Figures 11 and 12, the benefit of Cr (and similar elements like Al) can be explained using the solubility of Cr_2O_3 in molten Na_2SO_4. Despite the benefit of these elements in providing hot corrosion resistance, they cannot prevent accelerated attack, but they can delay its onset. Another important parameter in hot corrosion is the thickness of the salt film, the effect of which can be seen in Figure 30. A thin salt layer has a higher potential to cause accelerated attack than a thick salt layer.

3.3 Cr_2O_3 and Alkaline Earth Oxides in Hot Corrosion Resistance

The benefit of alloying Ni-base alloys with Cr for hot corrosion resistance is well known(4). As shown earlier in Figure 2, the presence of a Cr_2O_3-containing scale greatly increases the resistance to hot corrosion. The use of a Cr-containing additive for jet fuel has been investigated(25), and has been shown in a burner rig test to slow, but not prevent, hot corrosion

attack. Another study of Cr in hot corrosion-causing salts has shown that Na_2SO_4 melts with high amounts of chromium, *e.g.* $CrO_4^{2-}:SO_4^{2-}$ of 1:1, produced no accelerated attack(7). The same study, however, showed that small amounts of CrO_4^{2-} in a Na_2SO_4 melt can actually increase the rate of hot corrosion of pure Ni. The reasoning for this is that when there are chromate ions present in an Na_2SO_4 melt, cracks in the protective oxide scale produce locally reducing conditions where Cr_2O_3 is precipitated. When there is not enough CrO_4^{2-} to precipitate as Cr_2O_3, the cracks in the oxide provide sites for the penetration of sulfur into the alloy. As seen in Figure 10, at its minimum Cr_2O_3 shows a solubility of 2.4 moles of Cr ions per mole of Na_2SO_4. With an alloy that forms a Cr_2O_3-containing oxide layer in the presence of an Na_2SO_4 melt, it is possible to create, at least locally, a salt that contains enough Cr to prevent, or at least delay, accelerated attack. Modifying the TBC with Cr_2O_3 should result in the Cr_2O_3 dissolving into the salt before it reaches the ceramic/metal interface. This should increase hot corrosion resistance of the system as the dissolved CrO_4^{2-} ions do not come from the oxide layer on the metal. This is important because the condition of the bond-coat, and more specifically the top-coat/bond-coat interface, determines the spallation failure of the TBC(11).

It has been observed that the compositions of the salts deposited on gas turbine parts are not pure Na_2SO_4, but contain $MgSO_4$ and $CaSO_4$ and possibly other salts in addition to Na_2SO_4(16, 26). The Na_2SO_4-$CaSO_4$-$MgSO_4$ system forms a ternary eutectic with a melting temperature of 650°C. The liquidus projection of the phase diagram for this system is shown in Figure 13. The addition of alkaline earth (AE) oxides to the top-coat of a TBC system, as a complement to Cr_2O_3, is another way to modify the chemistry of the salt. In the presence of an Na_2SO_4-$CaSO_4$-$MgSO_4$

eutectic mixture, an AE oxide such as MgO or CaO would dissolve into the eutectic mixture. This would cause a shift away from the low-melting eutectic to a composition that is at least partially solid and possibly more viscous, inhibiting fast penetration of the salt through the top-coat. In the presence of pure Na_2SO_4, however, it is possible that the dissolution of AE oxides would cause a decrease in the melting temperature of the salt. In this study, when AE oxides are added to the top-coat, it will always be in addition to Cr_2O_3.

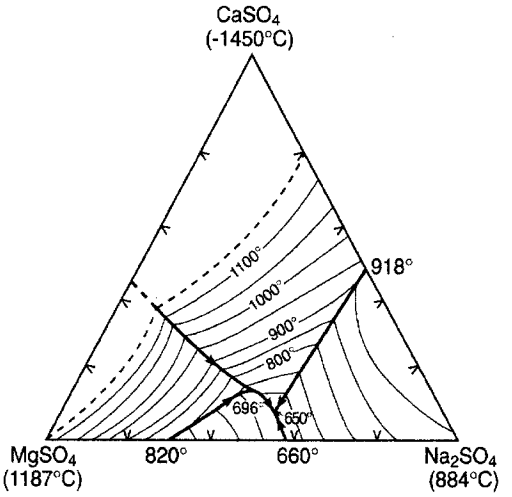

Figure 13. Liquidus projection of the Na_2SO_4-$CaSO_4$-$MgSO_4$ system (17).

3.4 Aims of Current Project

The primary goal of this research is to find a simple, economical, and effective method to modify the top-coat of a TBC system in a manner that will increase the hot corrosion resistance of the system. Other goals include:

- To devise one or more effective hot corrosion testing methods for TBC samples
- To determine stability under corrosion atmospheres of the two corrosive salts used in this study

- To observe the effect of salt layer thickness on accelerated hot corrosion attack
- To determine salt permeability of plasma-sprayed YSZ top-coat

Chapter 4: Experimental Procedures

The procedures used in this study include methods of coating formation, coating modification and hot corrosion testing. As mentioned earlier, all coatings were formed using APS techniques. Coating modifications included infiltration with aqueous solutions of water-soluble compounds of chromium (*e.g.*, chlorides, nitrates, acetates) and alkaline earth elements (*e.g.*, $MgCrO_4 \cdot xH_2O$) and modification of powders prior to forming. Hot corrosion testing included salt film, Dean Rig, and crucible tests. Salt film tests consisted of deposition of a salt film on the sample surface followed by isothermal heating of samples. Dean Rig tests took place in a controlled atmosphere with constant deposition of salt via a thermal gradient in the furnace. Crucible tests consisted of submerging a sample into a crucible of molten salt.

4.1 Coating Preparation

The APS coatings were prepared as a ceramic top-coat sprayed directly onto the Ni-200 or Haynes 214. The nominal composition of Haynes 214 is Ni-16Cr-4.5Al-3Fe in wt%. The use of an actual bond-coat was omitted as this study was concerned with the ability of a modified top-coat to change the molten salt so that the metal beneath it, no matter what it was, is less susceptible to accelerated attack.

4.1.1 Infiltration of YSZ Coatings

The porosity that is formed as the ceramic TBC layer is plasma sprayed offers a unique opportunity for modifying the chemistry of the coating. For

example, the coating can be submerged in an aqueous solution of a Cr- or Mg-containing compound. The solution infiltrates the entire coating, and when the water is dried out, the compound (e g. $MgCrO_4 \cdot xH_2O$) will be deposited on the surfaces of the interconnected pores. Upon further heating, the precursor compound will be converted to a stable, water-insoluble oxide in the coating. Experiments were carried out to determine optimal heat treating times and temperatures, and precursor solution concentrations and infiltration times that gave the greatest apparent converted infiltrant contents.

Three compounds, $MgCrO_4 \cdot 5H_2O$, $CrCl_3 \cdot 6H_2O$, and $Cr(NO_3)_3 \cdot 9H_2O$, were used as precursor compounds in this study. Prior to infiltration tests, the oxide precursor compounds were analyzed by thermogravimetric analysis (TGA) to determine the proper temperatures for drying and oxidizing these compounds. The heat treatments were limited to temperatures below 1100°C to avoid any excessive oxidation or destabilization of the alloy microstructure. Infiltration was accomplished by suspending coating samples in a wire basket submerged in a stirred solution for various times at room temperature. Following the infiltration, heat treatments were used to dry and oxidize the water-soluble precursor compounds present in the pores of the coating

Infiltration was also attempted by forced precipitation using the thermal decomposition of urea. This method has been used to successfully precipitate metal hydroxides, hydrous oxides and basic salts (27-30). The key to this uniform precipitation is the gradual change in pH due to the gradual release of ligands, like OH^-, CO_3^{2-}, and SO_4^{2-} (OH^- in this case), via the decomposition of urea (29). When the solution becomes basic enough,

the precipitating species becomes highly insoluble, so that extensive precipitation occurs. Solutions of $CrCl_3 \cdot 6H_2O$ were made in various concentrations, 26g/L to 240g/L, and urea was added to achieve a urea to $CrCl_3 \cdot 6H_2O$ molar ratio of 5 or 10. The solutions were heated and temperature was maintained at approximately 90°C until precipitation occurred.

4.1.2 Modified Starting Powders for Plasma Spraying

Another approach to the production of a top-coat containing oxides of AE metals or Cr is to modify the powders before the plasma spray process. A fine distribution of dopant oxides in the coating structure was desired. Several methods were employed to modify the YSZ powders, the first of which was much like the infiltration method described above. The powders used for this infiltration were Praxair AI-1075, an agglomerated and sintered ZrO_2-8wt.% Y_2O_3 powder. Agglomerated and sintered ZrO_2-8%Y_2O_3 powders were infiltrated with a 650 g/L solution of $CrCl_3 \cdot 6H_2O$ by pouring the powder into a stirred solution and allowing it to infiltrate for 30 minutes. The powders were then allowed to settle for 5-10 minutes, the solution was decanted into another beaker, and the powder was transferred into alumina crucibles. The powder was dried at 300°C for 30 minutes, and came out of the crucibles as a loosely bonded mass. This mass was crushed; half of the powder was run through sieves and removed for plasma spraying, and the other half was placed in the crucibles again for conversion at 800°C for 30 minutes. This was then crushed and run through sieves again. Coatings were made with both infiltrated powders.

The second method used to modify PAS powders was to begin with fine YSZ and Cr_2O_3 powders, nominally between 0.1 and 2.0μm particle size, blend them by wet milling in the presence of an organic binder and spray dry the blend into agglomerates. The average size of the agglomerates was 50μm, and the distribution used for plasma spraying was between 20μm and 106μm. Production of the spray-dried powder was carried out by a commercial vendor.

The third method was to arc-melt blended powders into a single mass which was then crushed to form powders suitable for plasma spraying. The fused and crushed powder was also produced by a commercial vendor, and the powders used for plasma spraying were smaller than 106μm. In addition to these powder-formation techniques, a physical blend of coarse YSZ and Cr_2O_3 powders (45μm to 75μm) was used.

All methods of powder modification, except infiltration, used a target composition of 8.8 wt. % (10 vol. %) Cr_2O_3. This composition was chosen because the average APS YSZ coating used in this study was produced with pore space of approximately 10 vol. %, so 10 vol. % is the absolute maximum amount of Cr_2O_3 that could be put into an as-sprayed APS YSZ coating. As a comparative reference, physically blended YSZ–10 vol. % Cr_2O_3 were deposited as APS coatings. This method, however resulted in a coarse distribution of Cr_2O_3 in the coating.

4.2 Hot Corrosion Testing

In hot corrosion studies, the relevance of laboratory corrosion tests to the attack observed in actual turbine engines is of major concern. In

attempting to reproduce conditions in a turbine engine, the high pressure burner rig is most accurate, but also quite expensive. A burner rig consists of a burner capable of burning fuel oils and producing a jet of combustion gases. Into this jet of combustion gases, impurities can be injected for the purpose of inducing hot corrosion. The test specimens are placed in the jet and rotated in the same way as the blades and vanes in a gas turbine engine. Many factors, such as combustion gas velocity, temperature, and composition and concentration of impurities, affect the corrosion of test specimens.

Some other tests used in the study of hot corrosion (crucible tests, electrochemical tests, furnace tests, etc.) have been discussed in the literature (31-33). The tests used in this study include the pre-deposited salt, crucible, and Dean Rig furnace tests as described in the following sections.

4.2.1 Pre-deposited Salt Tests

The pre-deposited salt test consisted of depositing a film of salt (usually 1-3 mg per cm^2 of coating surface area) on the test specimens via misting or droppering of a salt solution. In this study, salt solutions of 24g/L were used. These solutions were deposited using eyedroppers onto samples on a hot plate at approximately 120°C with a target salt deposition of 2 mg per cm^2. The specimens were then placed in a furnace at a fixed temperature for a prescribed time. In this study, the test specimens for the pre-deposited salt tests were coupons approximately 2 cm by 1 cm by 2 mm. Both uncoated substrates and samples coated on one side with a 100μm

thick APS YSZ top-coat were used. Typical samples can be seen in Figure 14.

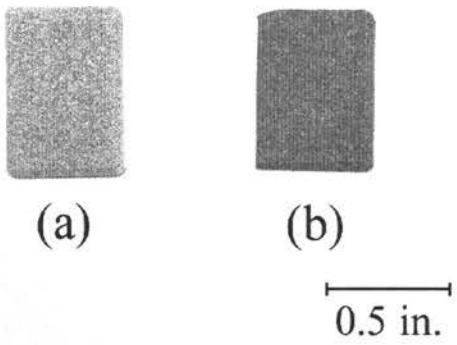

Figure 14. Coated coupons for hot corrosion testing: (a)coated with YSZ, (b)coated with physical blend of YSZ and Cr_2O_3.

These experiments consisted of the deposition of approximately 3 mg/cm^2 of salt followed by an isothermal heating at 900°C in air. Samples were heated and cooled slowly at the beginning and end of heating to reduce the effects of thermal cycling. Experiments also included the intermittent deposition of additional salt (~3 mg/cm^2 each 1- or 24-hour time period) in an attempt to maintain favorable conditions for accelerated attack. Both Na_2SO_4 and the ternary Na_2SO_4-$MgSO_4$-$CaSO_4$ eutectic were employed.

4.2.2 Crucible Tests

The crucible test is an experiment where the corrosion sample is either completely or partially submerged in a bath of molten salt. This test is usually considered very aggressive because of the amount of salt present. In this study, metal substrate samples for crucible tests were small rectangular pieces polished to 600 grit on both faces. The samples were

placed in Al_2O_3 crucibles with solid granular salt, and then heated to temperature. All top-coated crucible test samples were 1/4" pins approximately 5 cm long with hemispherical tips. The pins were coated with two thicknesses of coating (~100μm and ~300μm) so that the effect of coating thickness on hot corrosion attack could be observed. Typical samples are shown in Figure 15, and thick portion of the coating can be seen on the right-hand end of the samples. The samples were heated in the furnace outside the salt crucibles, and then placed directly into the molten salt at 900°C so that the salt covered approximately 3 cm of the coated end of the samples. The samples remained in the molten salt for some prescribed time and were then removed from the salt before the furnace was cooled.

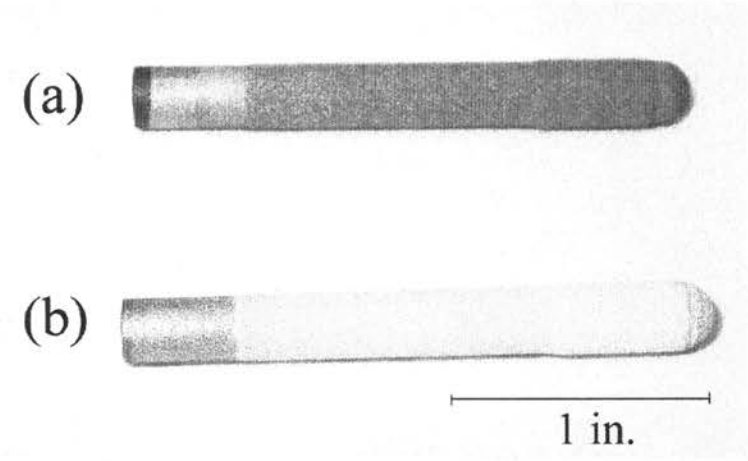

Figure 15. Coated crucible test samples: (a) Physical blend coating, (b) YSZ coating. The thicker portion of the coating can be seen on the right-hand side of the pins.

A variation of this test was employed to examine the effects of thermal cycling in the presence of molten salt on the corrosion resistance of the system and the integrity of the APS coating. It would be expected that differential volume changes between the coating and salt during a cooling

cycle could introduce stresses that crack the coating. In this variation, the samples were placed in the molten salt at 900°C for one hour, and then removed from the furnace and allowed to cool for about ten minutes. The cycle was repeated until the coatings fractured. All crucible tests in this study were conducted at 900°C in air.

4.2.3 Dean Rig Tests

The Dean Rig is a more elaborate furnace test. It consists of two temperature zones: a hot end where the salt is heated above its melting temperature and evaporates into the atmosphere and a cool end where the salt condenses on the test specimens. In the current study, the hot end of the furnace was set at 1050°C and the cool end at 900°C, as indicated in Figure 16. Along with this controlled thermal profile, a carrier gas of O_2-0.1% SO_2 was passed through a platinized honeycomb catalyst to form an equilibrium amount of SO_3 which, in turn, should stabilize the salt activity (see following section). This controlled atmosphere is also much closer than air to the conditions in a gas turbine. The samples used for Dean Rig tests were the same as those used in the pre-deposited salt tests. Preliminary Dean Rig tests showed very little salt deposition (*i.e.*, less than 0.1 mg/cm^2), so subsequent specimens were coated with a layer of salt, as in the pre-deposited salt tests, prior to heating.

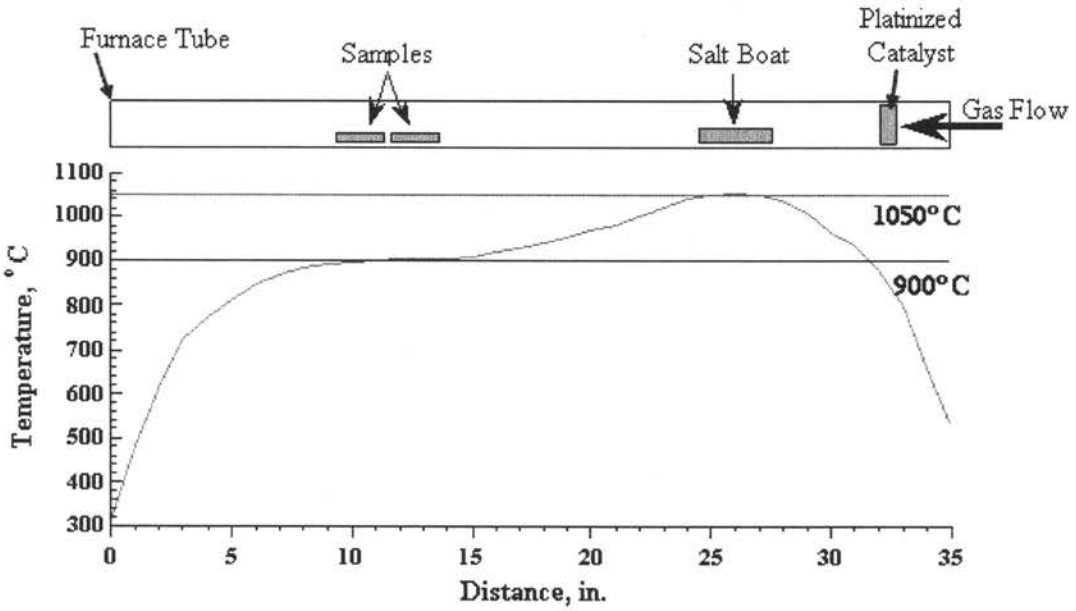

Figure 16. Controlled thermal profile of Dean Rig furnace with diagram of furnace tube, test specimens and boat of salt.

4.2.3.1 Dean Rig Atmosphere

A platinized honeycomb was included in the system to catalyze the formation of SO_3 from the O_2-0.1% SO_2 gas mixture.

$$2SO_2 + O_2 = 2SO_3$$

$$K(1173K) = \frac{P_{SO_3}{}^2}{P_{SO_2}{}^2 \cdot P_{O_2}} = 0.1077 \qquad (15)$$

From the equilibrium constant K (at 900°C) and the initial gas mixture composition (O_2-0.1% SO_2), the partial pressure of SO_3 at 900°C was calculated to be 2.47×10^{-4} atmospheres. This corresponds to $\log P_{SO_3}$ of -3.6, and by equation (11), $\log a_{Na_2O}$ of -13.1. This places the acidity of the

atmosphere just to the basic side of the Al_2O_3 and Cr_2O_3 solubility minima seen in Figure 10.

4.2.4 Salts Used in Corrosion Tests

As the presence of a molten or condensed salt is required for hot corrosion (14), a salt must be used in the aforementioned corrosion tests. Much work has been done on the chemistry of salts that cause hot corrosion (14, 16, 26). The work of Simons *et al.* (16) concerned the role of sodium sulfate, and DeCrescente and Bornstein (14) considered the mechanism of formation of sodium sulfate in gas turbine engines. More recently Bornstein and Allen (34) collected and measured the amount and composition of salt deposits on gas turbine components from different gas turbines operating near an ocean. Their results showed salt compositions near the ternary eutectic composition of the Na_2SO_4-$CaSO_4$-$MgSO_4$ system (seen in Figure 13). Two salts were used in the current study, the first being the ternary eutectic of Figure 13 and the second being Na_2SO_4. Na_2SO_4 was chosen for its well-known tendency to cause hot corrosion, and relative simplicity of chemistry. Reagent grade Na_2SO_4, $CaSO_4$, and $MgSO_4$ were used in hot corrosion tests and in the formation of the ternary eutectic. Salts were weighed and mixed in their as-received condition.

4.3 Analysis

Once tested, the specimens were evaluated using scanning electron microscopy (SEM), EDS X-ray analysis, XRD, and/or mass change data. It was also important to note that since the emphasis of this study was on the performance of thermal barrier coatings, the evaluation of test specimens

needed to be done carefully, as any crack or failure of the TBC could be considered a failure of the specimen. Hot corrosion is inherently a nonuniform attack. When quantifying this type of attack, difficulty arises in the selection of a representative region for measurement and in the measurement itself due to the roughness of the top-coat/metal interface from both grit-blasting and hot corrosion attack. A large standard deviation came about in this measurement from the dispersion of internal oxide and sulfide reaction products in the alloy. Characterization of the top-coat/metal interface was carried out by measuring the amount and depth of certain types of attack, shown in Figure 17.

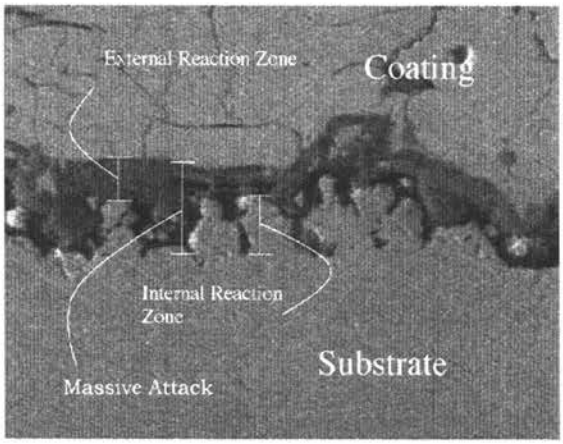

Figure 17. Illustration of the measurement scheme used in characterizing top-coat/metal interface. Haynes 214 substrate and untreated YSZ coating are shown.

Chapter 5: Results and Discussion

5.1 Sample Preparation

5.1.1 Infiltration of Coatings

Initial infiltration experiments consisted of immersing freestanding coatings (*i.e.*, coatings with substrate removed) in aqueous solutions of the oxide precursor compounds for various times and solution concentrations at room temperature. Three compounds, $MgCrO_4 \cdot 5H_2O$, $CrCl_3 \cdot 6H_2O$, and $Cr(NO_3)_3 \cdot 9H_2O$, were used. It was determined by TGA that all the compounds lost their waters of hydration by 300°C and were oxidized by 800°C. After infiltration, the samples were transferred to an Al_2O_3 tray and dried in a box furnace at 300°C for 30 minutes, followed by oxidation at 800°C for 30 minutes. Increasing infiltration time resulted in an increase in mass gain up to 30 minutes, above which, no appreciable increase in mass was observed. Increasing the solution concentration resulted in mass gain increases approximately up to the saturation point of each oxide precursor, Figure 18. The maximum mass gain was on the order of 4 to 6 mg of infiltrated oxide per gram of initial YSZ coating. The presence of this very limited residue could not be detected using X-ray diffraction (XRD) or energy dispersive spectrum (EDS) X-ray analysis. If all pores of a bulk piece of coating were to become completely filled with oxide from precursors, the mass gain would be on the order or 60 mg per gram of YSZ coating (based on the determination of 10% porosity).

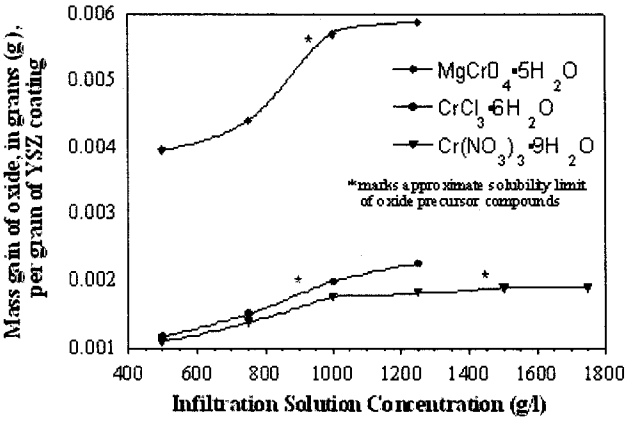

Figure 18. Mass gain of infiltrated YSZ coatings following conversion to oxide at 800°C for 30 minutes for the three different oxide precursor compounds.

In addition to the mass gain data collected during infiltration experiments, a freestanding coating was infiltrated with $MgCrO_4 \cdot 5H_2O$, dried and converted, and then chemically analyzed for Zr, Y, Mg and Cr. Assuming stoichiometric oxides, the amount of each oxide in the sample was calculated. The data in Table 2 show that oxides of Cr and Mg were present in the amount of about 4 mg/g of YSZ. This is in good agreement with the mass-gain data shown in Figure 18. The coating picked up a measurable amount of modifying oxide, probably in a very fine distribution throughout the pores of the YSZ coating. The fine distribution of the modifying oxides explains the inability of XRD and EDS to detect these oxides.

Table 2. Amount of oxides present in freestanding YSZ coating infiltrated once with $MgCrO_4 \cdot 5H_2O$ calculated from elemental chemical analysis.

Oxide	Wt %
Cr_2O_3	0.25
MgO	0.15
Y_2O_3	6.77
ZrO_2	92.82

The low mass gains from single infiltrations were not considered to be sufficient, so a method of multiple infiltrations was investigated. The multiple infiltrations were done with a solution of $CrCl_3 \cdot 6H_2O$ at 650 g/L. The samples were put through the heating cycle, described above, between each infiltration to avoid dissolving any previously infiltrated precursor. This multiple infiltration method resulted in a greater mass gain; however, 26 infiltration cycles produced only 50 mg of infiltrated Cr_2O_3 per gram of YSZ coating. Figure 19 shows the mass gained during the multiple infiltration experiment. This multi-step technique was considered too impractical to warrant additional attention.

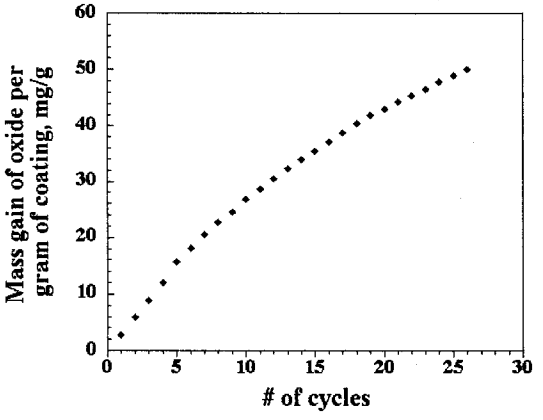

Figure 19. Mass gain of infiltrated YSZ coatings immersed multiple times followed by drying and conversion.

The next method of infiltrating YSZ coatings involved the forced precipitation of a Cr-containing oxide precursor using $CrCl_3 \cdot 6H_2O$ solutions of several concentrations ranging from 26 g/L to 240 g/L. The solutions of higher concentration, 240 g/L and 120 g/L, turned into crumbly, gelatinous masses when the urea decomposed. The lower concentration solution, 26 g/L, precipitated some particles, but did not result in appreciable mass gain. The forced precipitation experiments resulted in a maximum oxide

mass gain of only 0.5 mg per gram of YSZ coating and thus, this method of infiltration was abandoned.

5.1.2 Modified YSZ-based Starting Powders

APS coatings were produced from the four Cr_2O_3-containing powders discussed in Chapter 3: spray-dried, fused and crushed, infiltrated, and physical blend. The chemistry of the three processed powders and their coatings was determined using inductively coupled plasma mass spectrometry (ICP-MS). The results show that the coatings and the powders had nearly the same chemistry and that the coatings and powders of the spray-dried and fused and crushed forming methods were roughly of the target chemistry of 8.8 wt. % Cr_2O_3. These results can be seen in Table 3.

Table 3. Compositions of the modified starting powders determined by atomic emission. All results reported in wt.%.

	Composition, wt%		
Powder	ZrO_2	Y_2O_3	Cr_2O_3
Spray-dried	83.8	6.81	9.42
Fused and Crushed	83.4	8.93	7.65
Infiltrated	89.4	6.89	3.74
Coating			
Spray-dried	84.8	6.99	8.19
Fused and Crushed	85.4	8.52	6.04
Infiltrated	90.1	7.39	2.52

5.1.2.1 Spray-dried powders

Figure 20 shows the morphology and cross section of the spray-dried powders. The presence of Cr can be seen from the EDS data shown in Figure 20(c). The target composition of the spray-dried powder was 8.8

wt.% Cr_2O_3, and atomic emission analysis of the spray-dried powder showed 9.4 wt.% Cr_2O_3, Table 3. The presence of YSZ and chromia in the powder and coating was verified by X-ray diffraction, Figure 21, and chemical analysis, Table 3. Using typical APS parameters, the spray-dried powders were deposited as surface coatings shown in Figure 21(c). A significant number of the spray-dried agglomerates appear to have not completely melted in the plasma spraying process, so some of the porosity present in the powder was still present in the coating. This creates a high porosity TBC top-coat with poor mechanical properties. The high porosity provides more pathways for salt access. The poor mechanical properties allow the salt to crack the coating by differential volume changes upon heating and cooling.

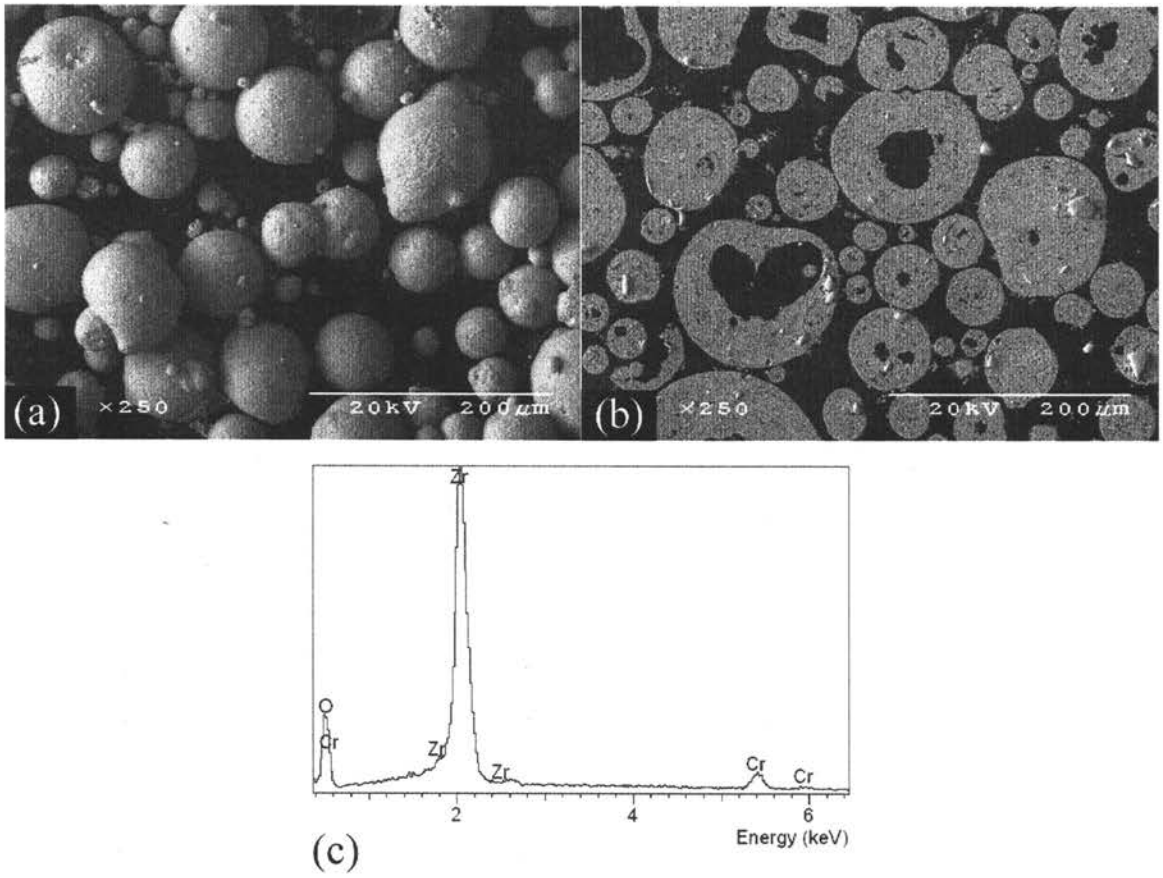

Figure 20. Micrographs of spray-dried (a) morphology and (b) cross section, and (c) EDS X-ray spectrum of spray-dried powder.

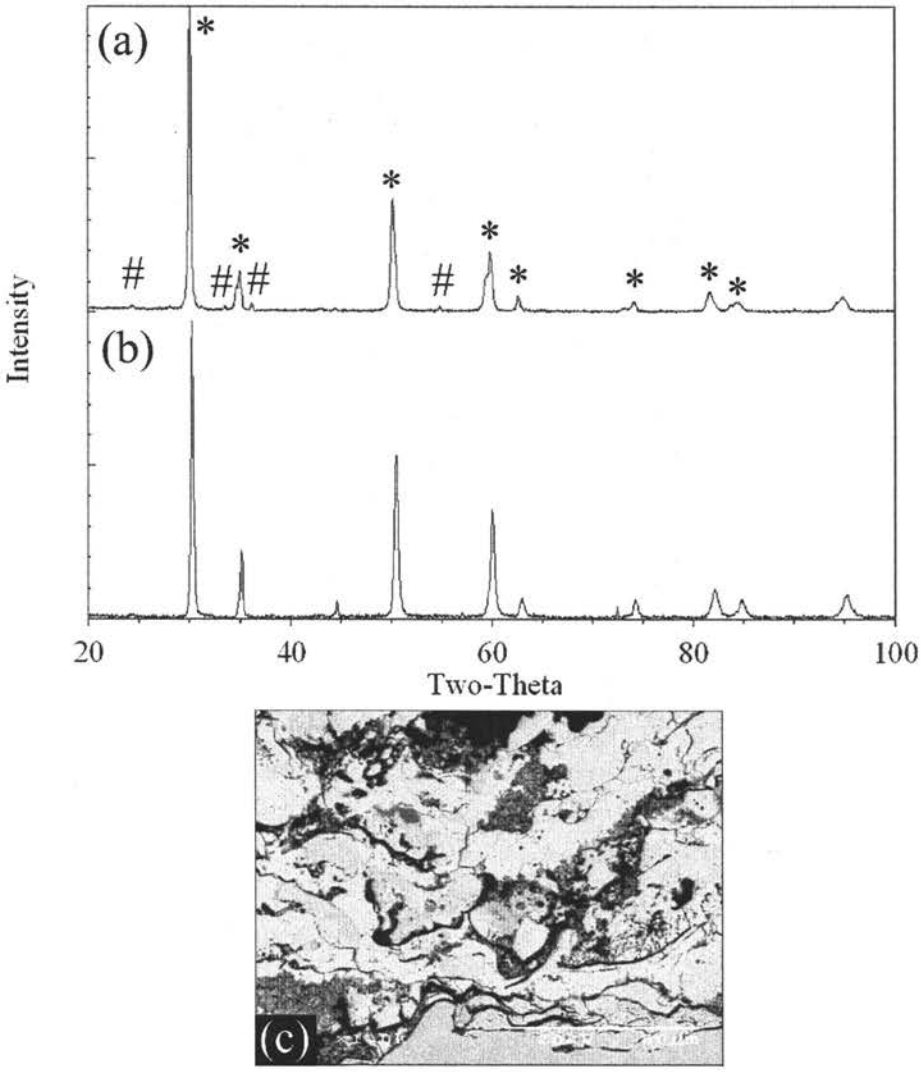

Figure 21. X-ray diffraction plot for (a) spray-dried powder and (b) coating made from spray-dried powder (tetragonal YSZ peaks are marked with *, and Cr_2O_3 peaks with #) and (c) cross section of APS coating.

5.1.2.2 Fused and crushed powders

Figure 22 shows that the fused and crushed powders were irregularly shaped due to the crushing process and were denser than both the spray-dried powders and infiltrated powders. These characteristics are common for fused and crushed material. Chemical analysis results show the fused and crushed powder contained 7.65 wt.% chromia, Table 3, which agrees

qualitatively with the XRD results in Figure 23(a). The XRD pattern for this powder also showed some small peaks for monoclinic ZrO_2, but they were not present in the XRD pattern for the coating, Figure 23(b). An example of the APS coatings obtained with the fused and crushed powders using the same parameters as for the spray-dried powders is shown in Figure 23(c). The XRD for this coating is shown in Figure 23(b). This coating is slightly less porous than that from spray-dried powders but still contains a lot of cracks and unmelted particles. The majority of the particles had melted and can be seen as flattened splats. The unmelted particles in the coating still have rough shapes, much like those seen in Figure 22(a). These dense unmelted particles can cause residual stresses in the coating which may induce spallation.

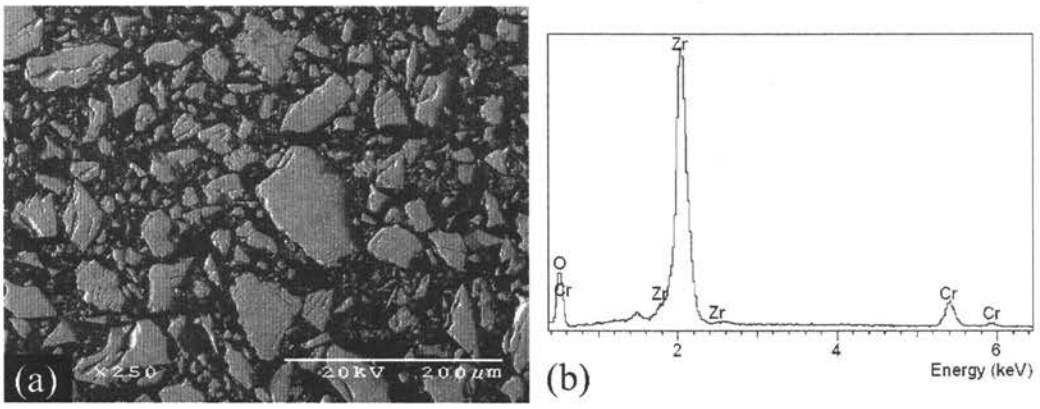

Figure 22. (a) Micrograph of fused and crushed cross-section and (b) EDS X-ray spectrum of fused and crushed powder.

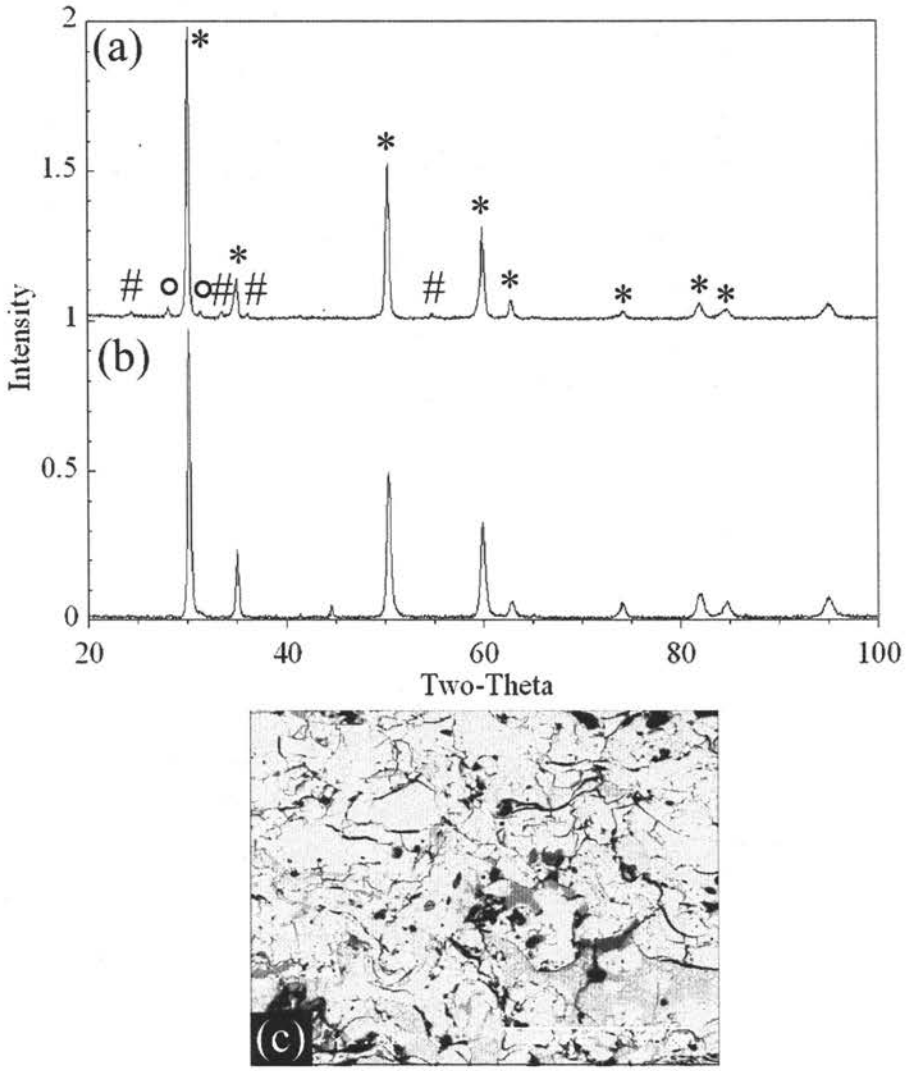

Figure 23. X-ray diffraction plot for (a) fused and crushed powder and (b) coating made from this powder (tetragonal YSZ peaks are marked with *, monoclinic ZrO_2 peaks with an o, and Cr_2O_3 peaks with #) and (c) cross section of APS coating.

5.1.2.3 Infiltrated porous YSZ powders

Infiltrated starting powders were produced as is described in Chapter 4. The cross section of a typical agglomerated and sintered YSZ particle after infiltration and conversion is presented in Figure 24. Chemical analysis showed the Cr_2O_3 concentration in the powder to be 3.74 wt.%, Table 3. X-

ray diffraction data for infiltrated and converted powder, Figure 25(a), and an APS coating from infiltrated powder, Figure 25(b), show approximately the same patterns as those for an as-sprayed YSZ coating, with the addition of several small peaks attributable to chromia. The XRD pattern for the infiltrated and converted powders showed a large amount of peaks for monoclinic ZrO_2, but these peaks were not present in the coating. The APS coating from infiltrated powder, shown in Figure 25(c), appears to have a bit higher porosity than in the as-sprayed YSZ coating, Figure. As with the coating from spray dried powders, Figure 21(c), high porosity would be expected to give rise to a higher number of salt ingress routes and decreased mechanical properties.

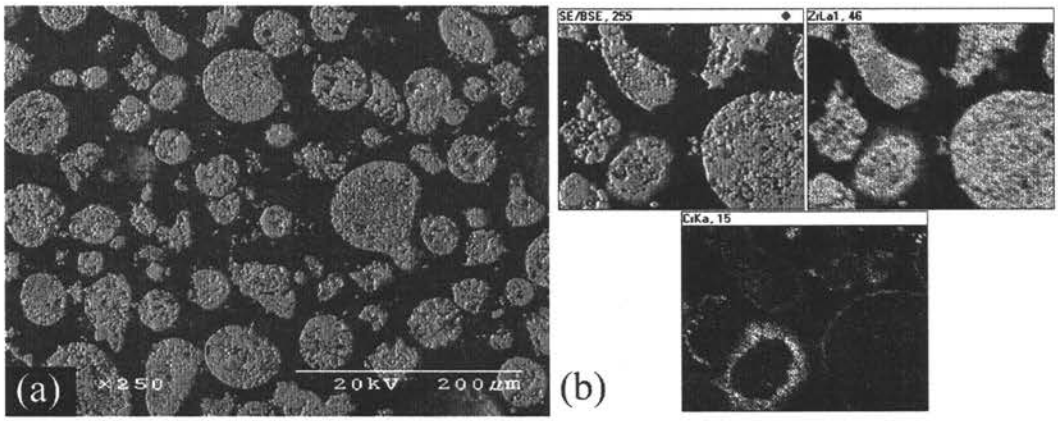

Figure 24. Micrograph of infiltrated powder cross-section (a), and EDS X-ray dot map showing Zr and Cr.

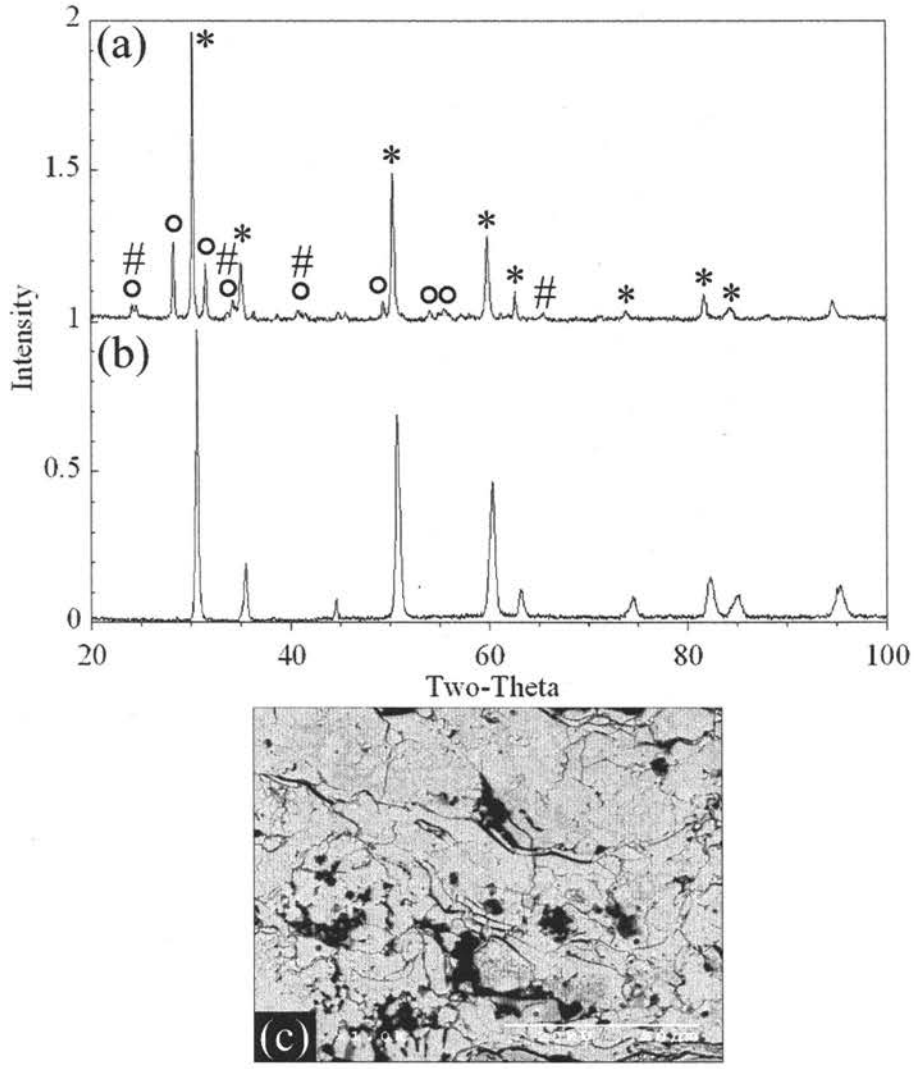

Figure 25. X-ray diffraction plot for (a) infiltrated and converted powder and (b) coating made from this powder (tetragonal YSZ peaks are marked with *, monoclinic ZrO_2 peaks with an o, and Cr_2O_3 peaks with #) and (c) cross section of APS coating.

5.1.2.4 Physical blends of YSZ and Cr_2O_3 powders

The physical blend produced a coarse distribution of chromia particles in the as-deposited coating, Figure 26. The XRD pattern of the physically blended powder shows a fair amount of peaks for monoclinic ZrO_2, but, again, these peaks were not present in the XRD pattern from the coating.

Chemical analysis was not performed on these coatings, but the XRD pattern in Figure 26(b), comparable to that seen with other the modified powders, confirms the presence of chromia. This was the only coating produced from a modified powder that had a microstructure nearly identical in crack and porosity distribution to an as-sprayed YSZ coating.

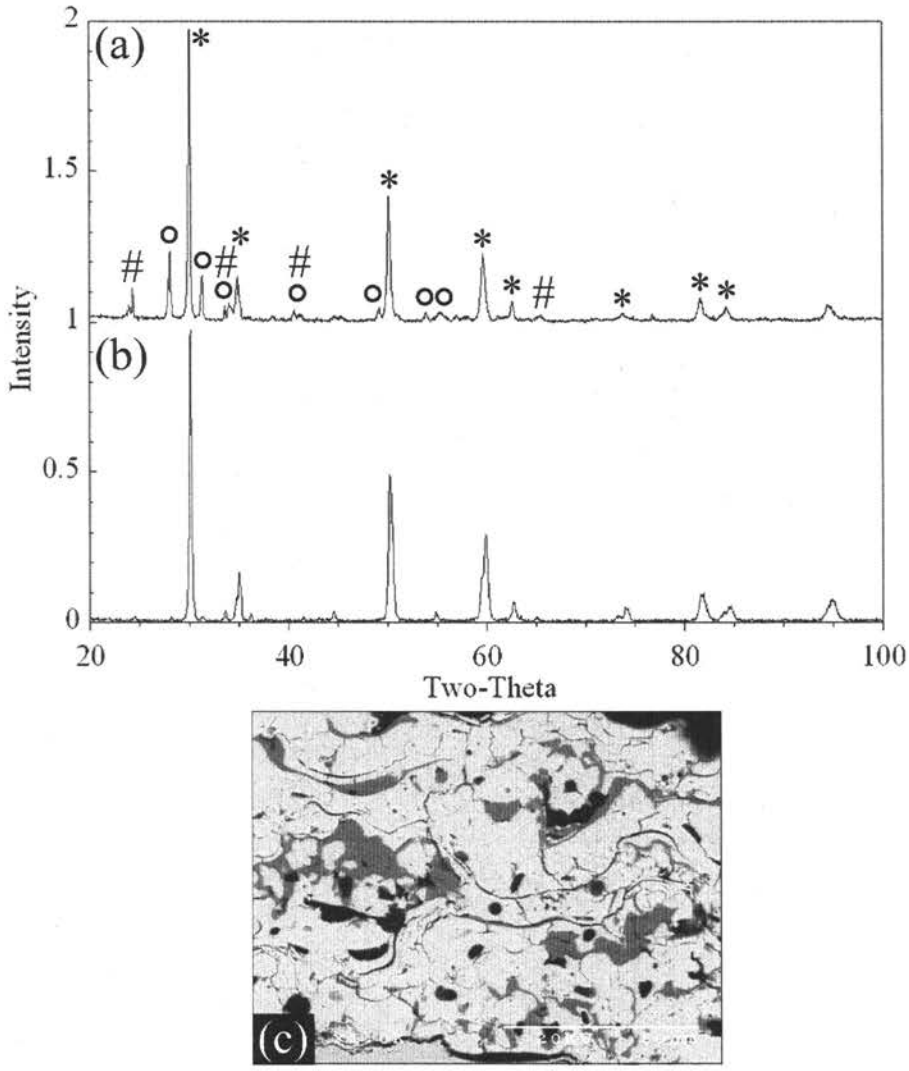

Figure 26. X-ray diffraction plot for (a) physical blend powder and (b) coating made from this powder (tetragonal YSZ peaks are marked with *, monoclinic ZrO_2 peaks with an o, and Cr_2O_3 peaks with #) and (c) cross section of APS coating.

5.1.2.5 Summary of Coatings Deposited from Modified YSZ-based Starting Powders

Of all the modified coatings discussed in this section, the only one with a microstructure very close to that of an as-sprayed YSZ coating is that produced from the physical blend of YSZ and Cr_2O_3. The coating from spray-dried powder had a large amount of porosity resulting from unmelted particles. The coating from fused and crushed powder had many cracks and dense unmelted particles. The coating from infiltrated and converted powder had higher porosity than an as-sprayed YSZ coating. The porosity and cracks in these coatings would presumably lead to an increased number of ingress routes for molten salt and decrease the mechanical properties. In addition, the unmelted particles in the coating from fused and crushed powders could produce residual stresses that could cause spallation of the coating. All these coatings were tested in Dean Rig experiments, the results of which are discussed in Section 4.3.4

5.2 Studies of Hot Corrosion Conditions

5.2.1 Stability of the Ternary Eutectic Salt

The eutectic composition of the Na_2SO_4-$CaSO_4$-$MgSO_4$ system melts at 650°C, and any shift in composition of the sulfate mixture (*i.e.*, via selective oxidation or losses) would result in an increased liquidus temperature. Eutectic salts were formed by the following four heating methods to create a solidified mass of salt:

1) The constituents were mixed in eutectic composition, placed in an alumina crucible, and then heated in air at 850°C.
2) Salt formed in the same manner as 1) except that an alumina lid was placed on the crucible.

3) Salt formed in the same manner as 1) except heated under a catalyzed O_2-0.1% SO_2 atmosphere.
4) The constituents were mixed in eutectic composition and dissolved in water. The water was boiled off and the remaining salt was placed in an alumina boat. The distillate salt mixture was then heated under a catalyzed O_2-0.1% SO_2 atmosphere at 850°C.

The salts were heated at 850°C for 30 min and cooled to form a solid mass. Additional tests were executed with heating times of 12 hours to determine long-term stability of the eutectic.

Chemical analysis of the salts processed by the four methods showed that they were all very close to the eutectic composition. The measured compositions are shown in Table 4, and their respective positions on the liquidus projection in Figure 27. Thus, the method of processing the ternary eutectic from its constituents prior to use in hot corrosion tests does not appear to matter. For the hot corrosion tests in this study it was decided to deposit the ternary salts on sample surfaces by dissolving the three constituents in an aqueous solution, then depositing the solution on samples heated to ~120°C on a hot plate. In the 12-hour heating period, which was investigated for forming methods 1 and 4, loss of $CaSO_4$ was observed (Table 4). In air at 1atm at 1200K, the formation of CaO in either gaseous form, Equation 16, or solid form, Equation 17, from pure, solid $CaSO_4$ is unfavorable.

$$CaSO_{4(s)} = CaO_{(g)} + SO_{3(g)}$$
$$\Delta G(1200K) = 658.5\,{}^{kJ}/_{mol} \qquad (16)$$

$$CaSO_{4(s)} = CaO_{(s)} + SO_{3(g)}$$
$$\Delta G(1200K) = 186.9\,{}^{kJ}/_{mol} \qquad (17)$$

These calculations pertain to pure solid $CaSO_4$ and air at atmospheric pressure, but experiments took place with a liquid Na_2SO_4-$CaSO_4$-$MgSO_4$ eutectic mixture both in air and in a catalyzed O_2-0.1% SO_2 gas mixture at 1atm. Apparently, the liquid ternary salt melt creates conditions for the loss of Ca, but the atmosphere has no effect on the loss. These observations show that the conditions used for hot corrosion testing in this study result in a variable salt composition of the Na_2SO_4-$CaSO_4$-$MgSO_4$ eutectic salt.

Table 4. Results from chemical analysis of eutectic salt formation methods.

	30-min Forming Method				12-h Forming Method	
Constituents	1	2	3	4	1	4
Na_2SO_4	56.00	56.90	54.70	57.40	55.28	55.33
$CaSO_4$	7.17	7.01	7.32	7.42	1.90	2.00
$MgSO_4$	37.13	36.46	38.61	37.35	42.82	42.67

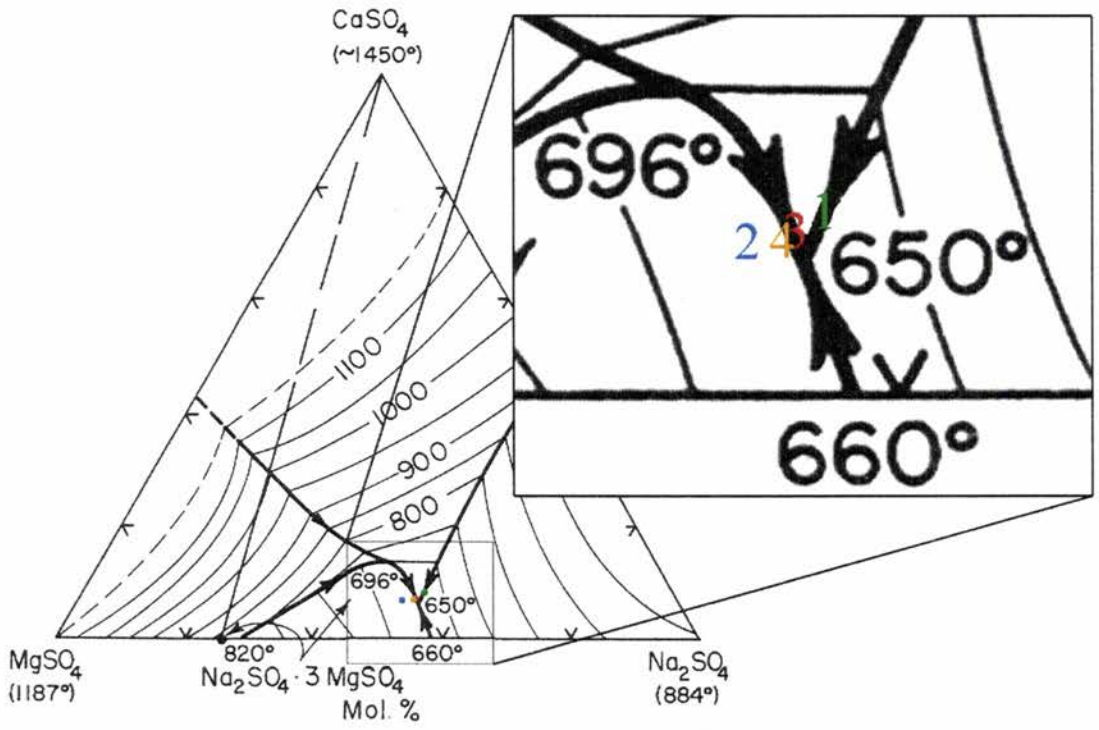

Figure 27. Eutectic phase diagram with compositions of various methods of forming.

5.2.2 Effect of Salt Thickness and Cr_2O_3 Content

The effect of the salt layer thickness on accelerated hot corrosion attack was investigated using the crucible test. Haynes 214 coupons were either completely or partially submerged in either Na_2SO_4 or Na_2SO_4 with 10 wt.% Cr_2O_3. Partially submerging samples in Na_2SO_4 results in the forming of a thin salt film over the surface of the specimen as the salt wets the alloy. It was observed that completely submerged samples incurred no accelerated attack up to 72 hours in a 900°C molten Na_2SO_4 bath. These samples, shown in Figure 28, sustained only small localized areas of degradation. In contrast, partially submerged samples underwent breakaway attack at approximately 12 h for Na_2SO_4 and 22 h for Na_2SO_4 with 10 wt.% Cr_2O_3. These results are shown in Figure 29.

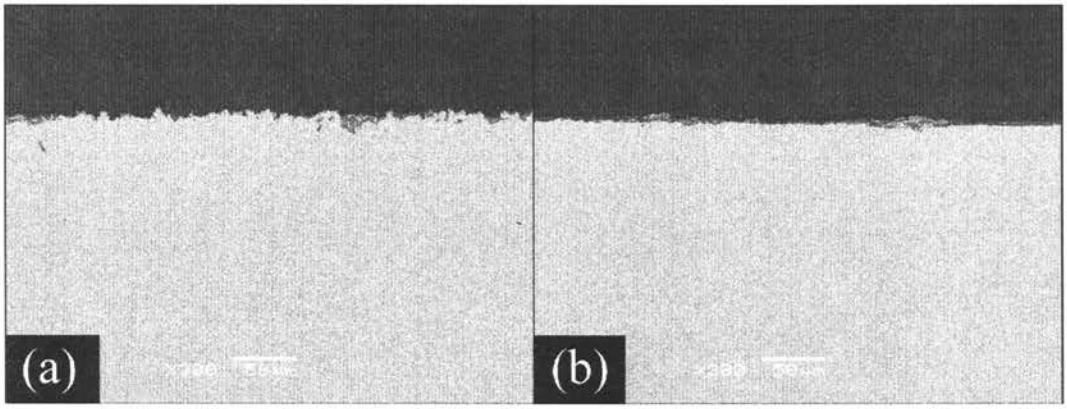

Figure 28. Samples from crucible test, completely submerged (a) in Na_2SO_4 for 72 hours and (b) in Na_2SO_4-10wt.% Cr_2O_3 mix fom 44 hours.

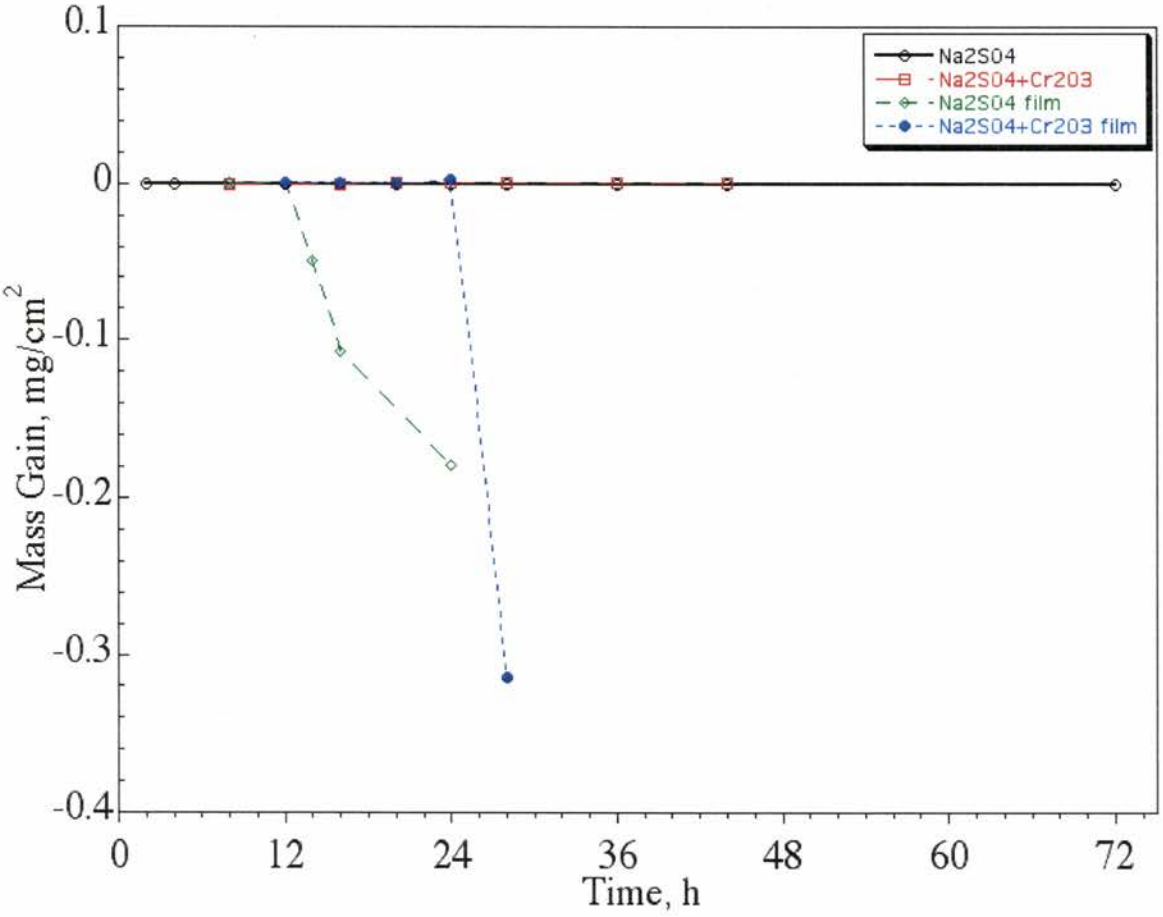

Figure 29. Mass change of Haynes 214 coupons in crucible tests.

The results of these tests show that a thin layer of salt can be much more detrimental than a deep melt. Even if a positive solubility gradient is formed, as illustrated for a Cr-containing oxide scale in Figures 11 and 12, accelerated attack is still possible. As the oxide is dissolved, a gradient in $[AlO_2^-]$ can develop across the salt layer. At the Na_2SO_4/oxide interface, $[AlO_2^-]$ is fixed by the kinetics of dissolution and the solubility limit of Al_2O_3 in Na_2SO_4. At the Na_2SO_4/gas interface, AlO_2^- can react to precipitate Al_2O_3 by Equation 18. At this point, $[AlO_2^-]$ is fixed by the kinetics of this reaction and the P_{O_2} in the surrounding atmosphere.

$$2AlO_2^- = Al_2O_3 + \tfrac{1}{2}O_2 \qquad (18)$$

With a thin salt layer, the [AlO_2^-] gradient can be very steep, resulting in a large diffusional driving force, Figure 30(a). For a thick salt layer, in the same atmosphere, the gradient will not be as steep, and the diffusional driving force will be less, Figure 30(b). If a positive solubility gradient is formed, attack would be expected to occur faster with a thin salt layer than with a thick layer, as demonstrated in Figure 29.

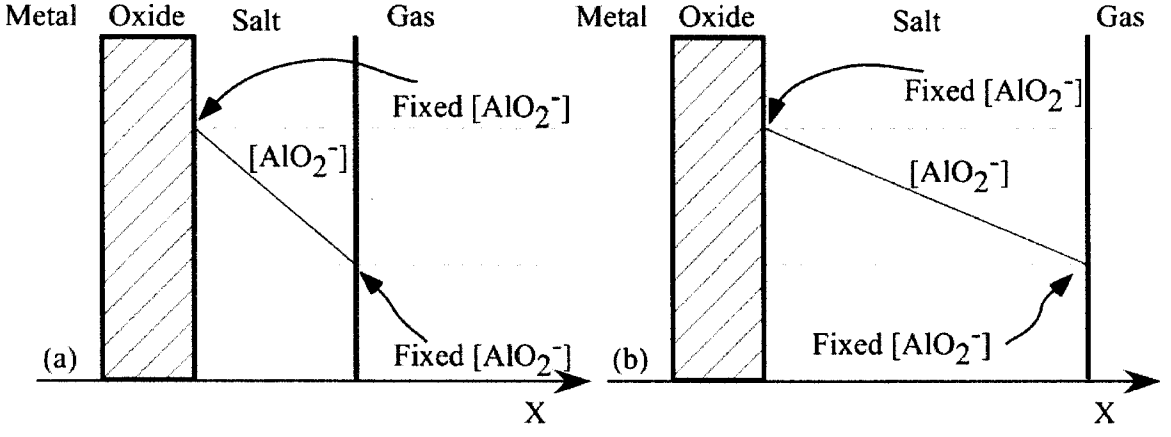

Figure 30. AlO_2^- concentration gradient present in molten Na_2SO_4 (a) thin layer and (b) thick layer

For the partially submerged specimens, a longer incubation period was observed when the salt contained Cr_2O_3. This shows that when accelerated attack does occur, *e.g.*, for a thin salt film, Cr in the salt has the ability to delay the onset of accelerated attack. Figure 31 shows samples before and after the onset of accelerated attack. As illustrated in Figure 31(a) and (b), the appearance of a sample can go from nearly pristine to severely corroded with a large amount of internal Cr-rich sulfides in as little as 2 hours.

A distinctive morphology was observed in the corroded samples just before the onset of accelerated attack and can be seen in Figure 32. Specifically,

needle-like particles formed in a uniform manner over flat regions of the specimen surface. In Addition, small sulfides can also be seen in the left-hand side of Figure 32(a) away from the needles. The needles were found by EDS analysis to be an Al-containing oxide. It is presumed that as the salt fluxes the Al_2O_3 scale and the scale is replenished, the alloy becomes depleted in Al so that it can no longer form an Al_2O_3 scale. At this point, Al begins to oxidize internally because it is not present in high enough concentrations at the surface, and it is the most thermodynamically stable oxide possible in the system

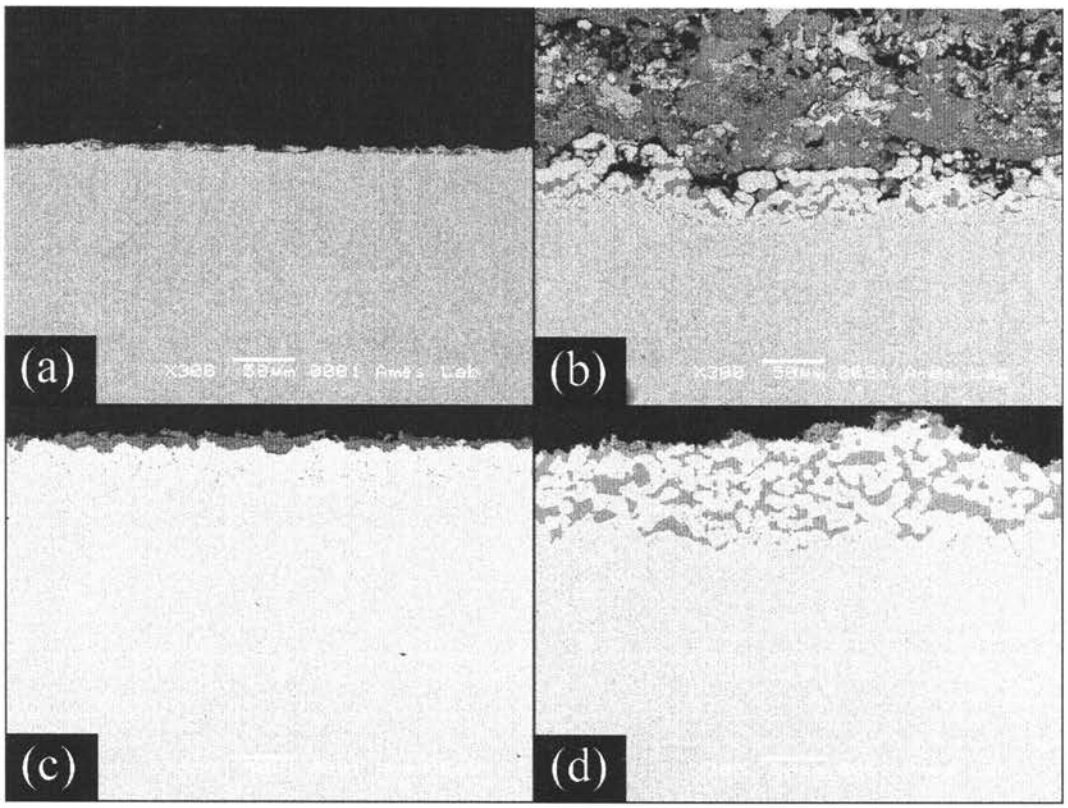

Figure 31. Samples from partially submerged crucible test with Na_2SO_4, (a) 12 h and (b) 14 h and with Na_2SO_4-10wt.%Cr_2O_3 mixture, (c) 24 h and (d) 28 h.

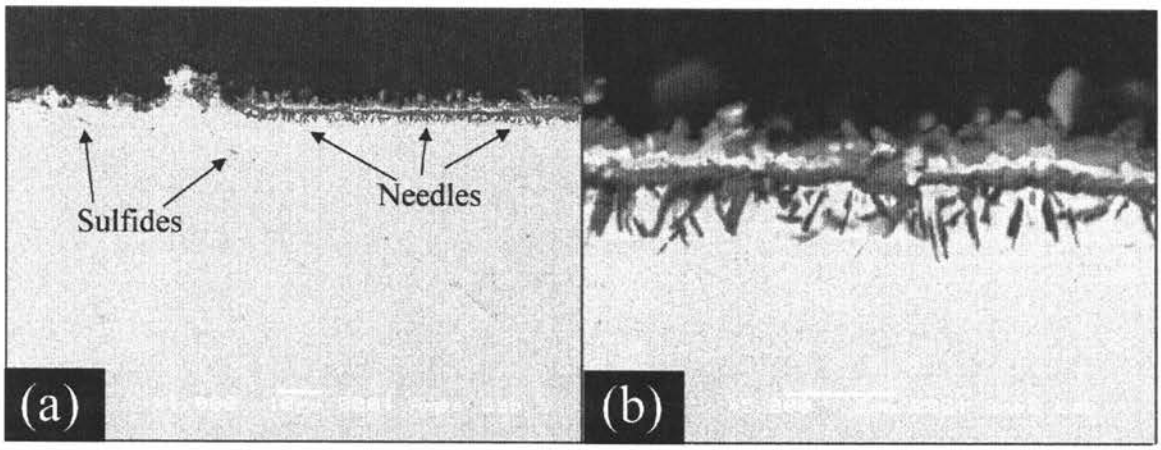

Figure 32. Needle-type morphology observed in crucible test with samples partially submerged in Na_2SO_4-10wt.% Cr_2O_3 mix for 20 h., (a) 1000x micrograph showing needles adjacent to area with small sulfides and (b) 5000x micrograph showing needles.

5.2.3 Molten Salt Permeability of Coating

The ability of the salt to permeate the coating was investigated using a YSZ crucible formed by APS with walls approximately 3mm thick. The crucible was filled with Na_2SO_4 and placed in a catalyzed O_2-0.1% SO_2 atmosphere on an Al_2O_3 tray at 900°C for 4 hours. When the crucible was removed from the furnace, the inside salt level had decreased noticeably and there was salt present in the alumina tray. Upon SEM examination, Na_2SO_4 was observed in pores near both the inside and outside walls of the crucible. A thin layer of salt was also observed along both walls, and indicated in Figure 33.

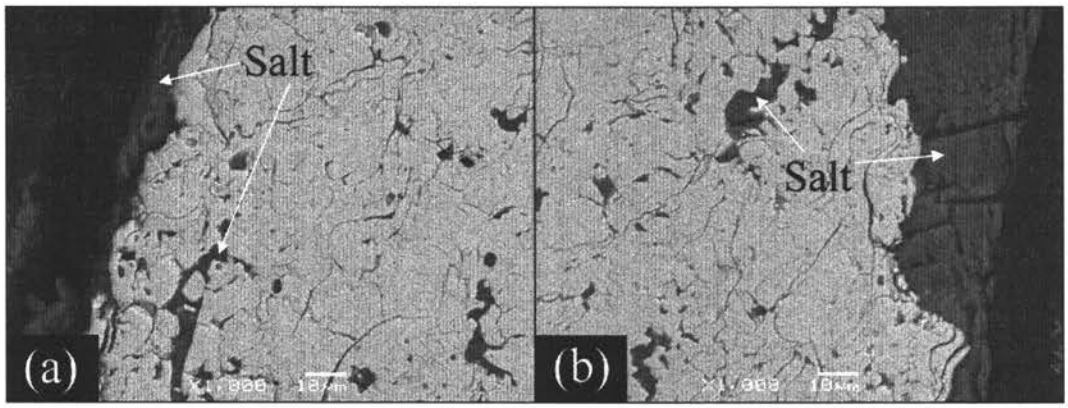

Figure 33. Micrographs showing (a) inside wall and (b) outside wall of APS formed YSZ crucible after containing Na_2SO_4 for 4 hours in catalyzed O_2-0.1% SO_2 atmosphere at 900°C.

This result shows that molten Na_2SO_4 at 900°C can permeate a 3mm coating in less than 4 hours, so the hot corrosion resistance contributed to a TBC system by an untreated top-coat has very little, if anything, to do with the ability of the salt to penetrate through it. The resistance associated with a TBC top-coat most likely follows from the limited amount of substrate (or bond coat) surface area (about 10% from the porosity of the top-coat) available for the salt to contact. With the limited amount of free area at the interface and limited amount of free space in the coating, a small amount of salt can be regarded as a thick layer (*i.e.*, a relatively long distance between the salt/oxide interface and the salt/gas interface).

5.3 Hot Corrosion Testing of TBC Samples

In the current work, three types of hot corrosion tests were conducted: pre-deposited salt, Dean Rig, and crucible furnace tests. Each of these tests was performed in several variations. As these tests were designed to cause accelerated hot corrosion attack, it is important to compare test specimens to as-sprayed coatings and specimens that underwent oxidation without

salt. These two baseline specimens are shown in Figure 34. The as-sprayed specimen, 34(a), shows an intimate interface between the coating and substrate. The specimen oxidized without salt shows the same type of intimate interface, but has grown an oxide layer, probably of Al_2O_3 and Cr_2O_3, between the coating and the substrate.

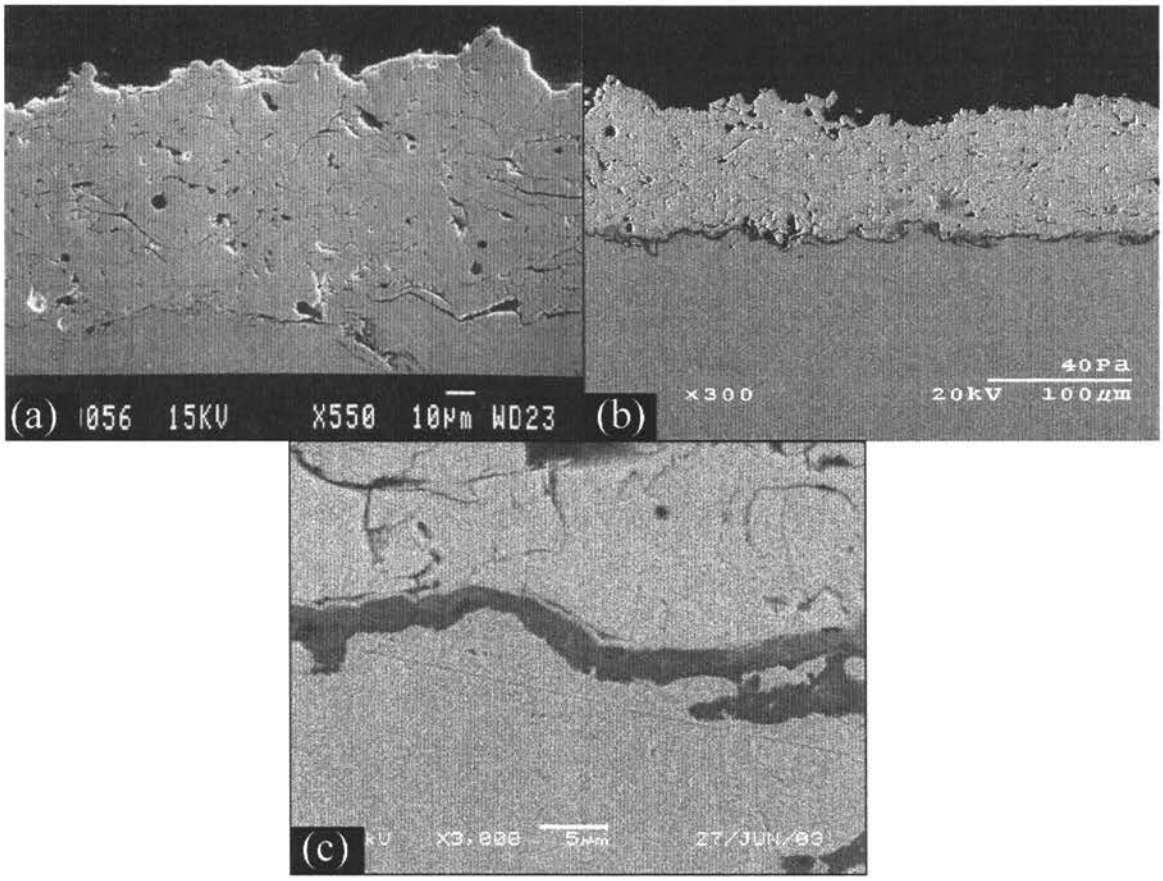

Figure 34. Baseline specimens of (a) as-sprayed YSZ coating, (b) low magnification, and (c) high magnification of as-sprayed YSZ coating oxidized ten 24-hour cycles without salt.

5.3.1 Pre-deposited Salt Tests with Ternary Eutectic

The initial pre-deposited salt tests used the ternary eutectic salt as a corrodant, and were carried out in air for 10 24-hour cycles with a

redeposition of salt at the beginning of each cycle. Each cycle consisted of a slow heat and slow cool to reduce the effects of thermal cycling on the samples. The results of this preliminary test showed little to no attack on the majority of the specimens. Mass gain data was collected during these tests, but the only conclusive result was that the coatings infiltrated with $CrCl_3 \cdot 6H_2O$ accrued more mass of corrosion product than any of the other specimens. The amount of attack for these 10-cycle specimens was measured in the manner shown in Figure 17, and the results are shown in Figure 35.

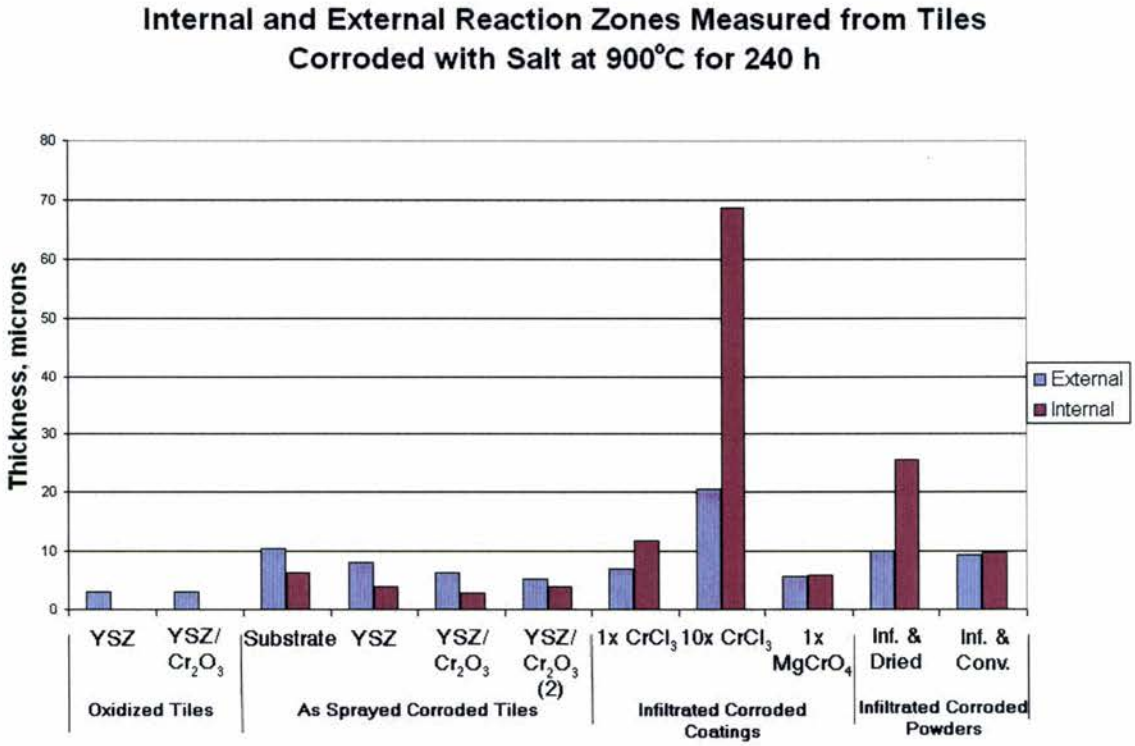

Figure 35. Plot showing the depth of external and internal oxidation in samples from 240-hour pre-deposited salt tests with eutectic salt.

The $CrCl_3 \cdot 6H_2O$-infiltrated samples showed the deepest attack, and were the only specimens to show the morphology of accelerated attack. The coatings

with multiple infiltrations (10 infiltrations with $CrCl_3 \cdot 6H_2O$) failed by coating spallation, some coatings completely delaminating from the substrate, accompanied by voids and severe corrosion on coated and uncoated portions of the alloy. An example of this is shown in Figure 36.

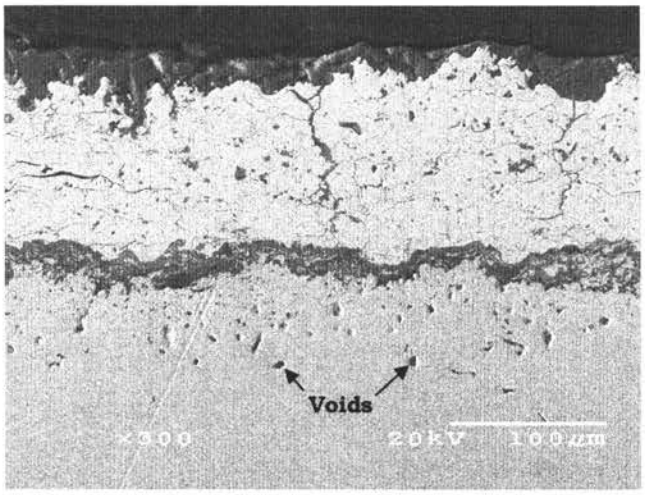

Figure 36. Haynes 214 substrate with 10x $CrCl_3$-infiltrated YSZ coating after 10 24-hour predeposited-salt corrosion tests with eutectic salt. Voids in substrate are indicated.

The coating failure is believed to be due to a combination of cracks induced in the thermal cycling of the infiltration process and the effects of the molten salt. The severe corrosion is believed to be due to residual Cl from the infiltration of the coating. Chlorides, whether in solid or vapor phase, are known to produce spalling of protective oxides(35). It has been suggested that volatile oxychlorides or chromates, due to the presence of chloride at the scale/metal interface, could cause this spalling(35). The formation of internal voids has also been observed after exposure to Cl-containing atmosphere at 900°C(36). The rest of the coatings showed small amounts of attack, but no accelerated hot corrosion.

It also appears in the micrographs of the test specimens that the accumulated salt after multiple applications and 24-hour heating cycles oxidized or decomposed to form a solid surface layer, which prevented subsequent salt applications from penetrating through the coating to the substrate interface, thus decreasing the severity of the test. On uncoated substrates, a similar solid surface layer was observed. Figure 37 shows a micrograph and EDS X-ray dot maps illustrating the solid layer and the separation of elements from the ternary eutectic salt. It is clear from the distribution of Na, Ca, Mg, and S throughout the pores that the salt is making its way into the coating, but not accumulating at the coating-substrate interface.

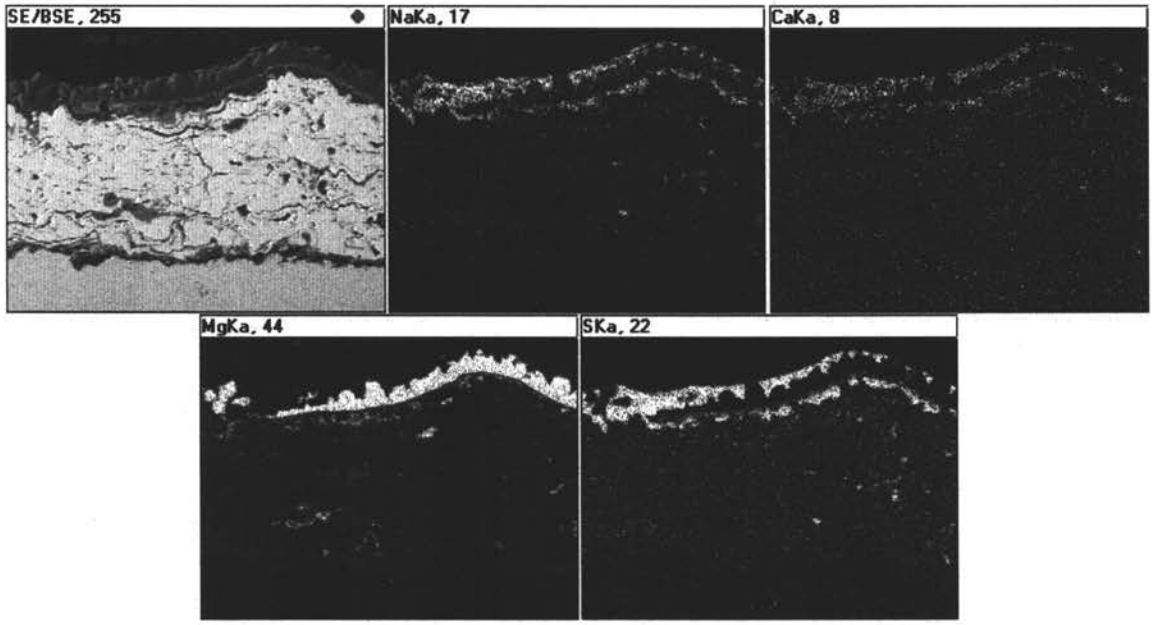

Figure 37. EDS X-ray dot maps for Na, Ca, Mg, and S in coating made from physical blend, YSZ – 10 vol. % Cr2O3, and tested ten 24 hour cycles with ternary eutectic salt using the pre-deposited salt method.

An attempt was made to characterize this layer using X-ray diffraction. Each XRD plot of data from samples that had this layer showed three

intense peaks in addition to those for YSZ. Three peaks were found to correspond to MgO in its periclase structure. An example of an XRD pattern is shown in Figure 38, with MgO peaks and YSZ peaks indicated.

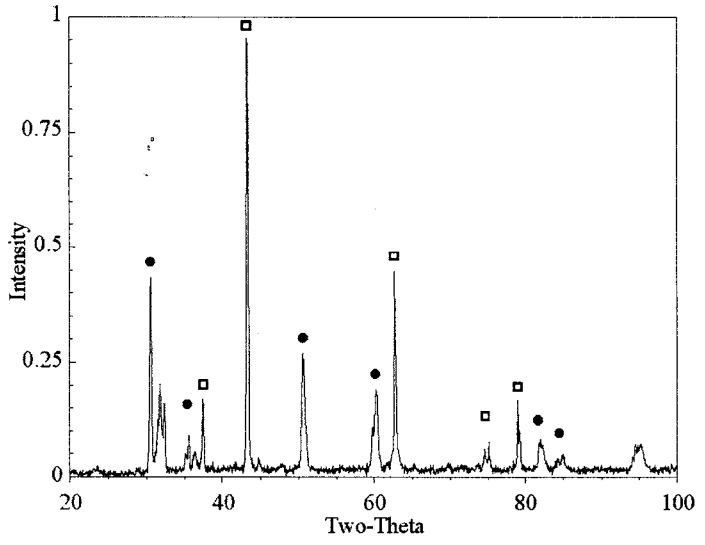

Figure 38. XRD of the coated surface of a YSZ-coated sample corroded 10 24-hour cycles with ternary eutectic salt at 900°C in air. Peak standards for MgO (□) and YSZ (•) are included.

It was initially thought that the $MgSO_4$ was decomposing because of the ambient air atmosphere and/or the relatively long exposure time, 24 hours, at 900°C. In an attempt to forestall this decomposition, the time at 900°C was reduced to 1 hour per cycle and salt was replenished each hour so as to maintain a nearly eutectic salt composition. This test was carried out to 72 hours without any accelerated mass gain or extreme changes visible to the naked eye. Seen in Figure 39, a thick layer of the ternary salt was observed on these samples, but formation of a capping layer of MgO was not observed. There was also very little reaction between the bare substrate and the salt, as is seen in Figure 39(a). Figure 39(b) shows an as-sprayed YSZ coating tested 72 one-hour cycles; the thick solid layer is clearly present above the coating. The constituents of the ternary eutectic salt, S, Mg, Na,

and Ca, were found in pores of the test specimen coatings using EDS X-ray analysis, but this clearly did not cause accelerated attack.

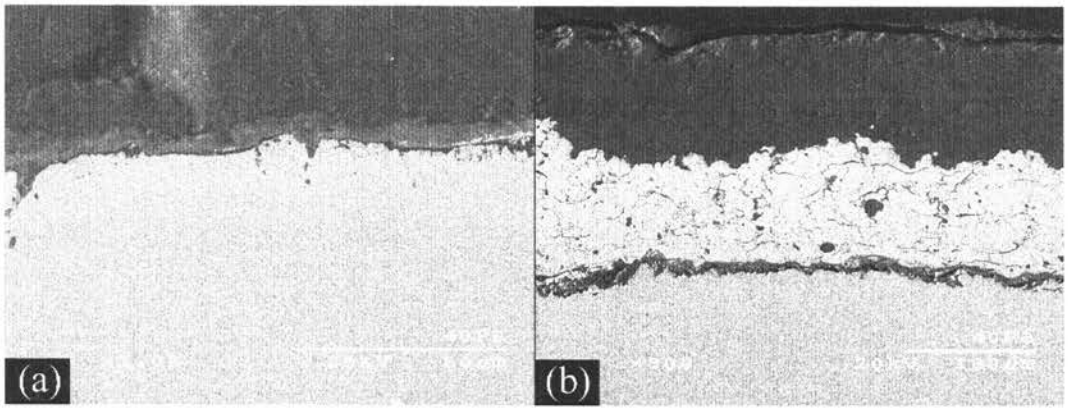

Figure 39. Specimens tested 72 one-hour cycles with the ternary eutectic salt using the pre-deposited salt method. (a) Bare substrate showing very little reaction (1000x). (b) As-sprayed YSZ coating with thick solid layer (300x).

5.3.2 Pre-deposited Salt Tests with Na_2SO_4

Na_2SO_4 was used because it is more stable at 900°C than an $MgSO_4$-containing salt and it has a much simpler chemistry than the ternary eutectic. The test specimens underwent only 2 one-hour cycles before the salt began turning yellow during deposition. The yellow color is inferred to come from water soluble chromate, CrO_4^{2-}, ions when the salt reacts with the Cr_2O_3 in the coating, or on the surface of the alloy. Accelerated attack of bare substrates began after 16 one-hour cycles and the coating on the as-sprayed YSZ specimen began delaminating after 26 hours. The physical blend coatings remained intact through 26 cycles.

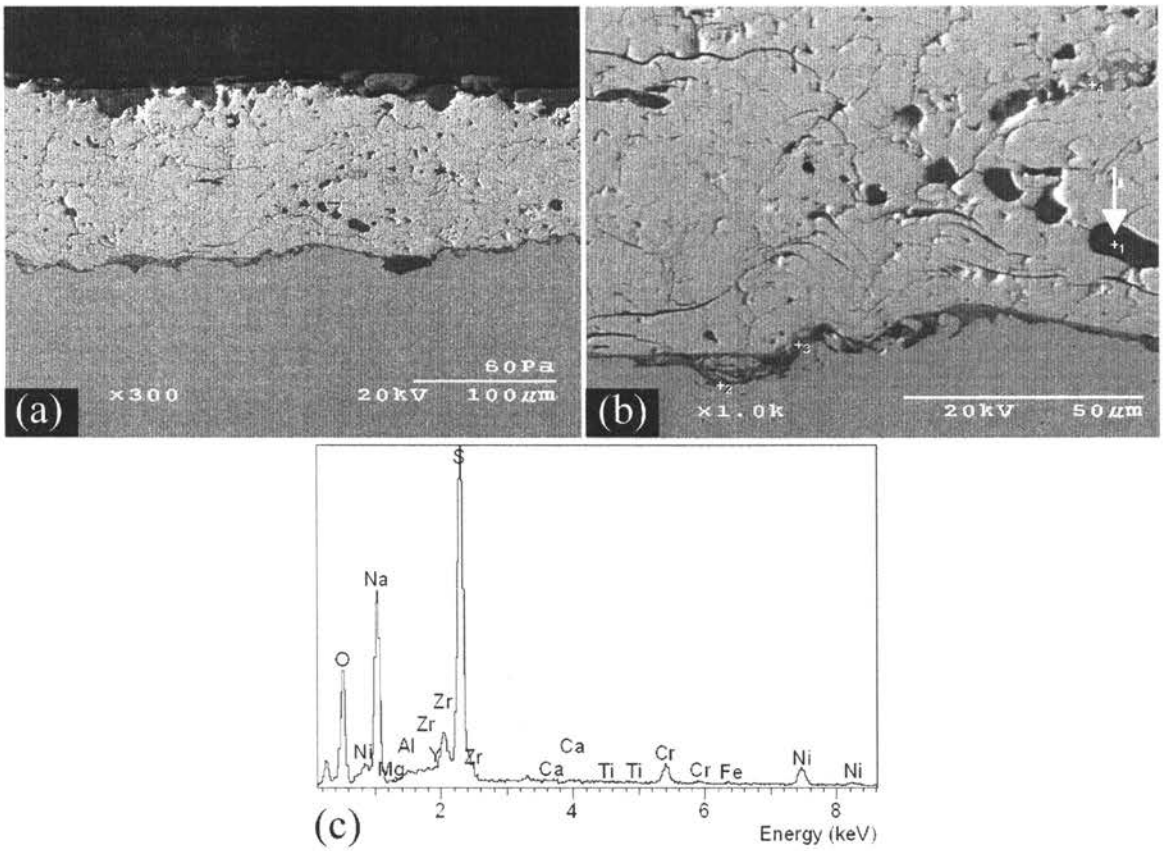

Figure 40. YSZ coating tested with Na_2SO_4 for 26 one-hour cycles at 900°C at (a) 300x, and (b) 1000x. EDS X-ray spectrum (c) shows mainly S, Na, and O in pore at far right of (b), marked with an arrow.

Figure 40(a) shows an as-sprayed YSZ coating that underwent 26 one-hour cycles at 900°C in the presence of Na_2SO_4. No accelerated attack was observed, but the salt layer above the coating is not as thick as was observed in the same test with the ternary salt. Also, salt was present in pores deep in the coating, as is indicated by the arrow in Figure 40(b) and verified by the corresponding EDS analysis in 40(c). Delamination of the edges and corners of the untreated YSZ coating was observed after 26 1-hour cycles, and was probably caused by the CTE difference between the salt and the ceramic, and the ability of the salt to access the alloy at the edges of the coating. This test showed that the effects at the edges of the

coating are significant and that the APS coating, away from the edges of the sample, is a good inhibitor of accelerated hot corrosion attack, *i.e.* the uncoated alloy underwent accelerated attack after 16 hours, but the coated sample showed no accelerated attack after 26 hours.

5.3.3 Dean Rig Tests

Initial Dean Rig tests included bare substrates, as-sprayed, and infiltrated coatings. Al_2O_3 discs were used to determine the salt deposition rate. Samples were placed in the furnace for 24-hour periods then removed and weighed; this was repeated for a total of five days. The salt deposition rate on the Al_2O_3 discs was almost immeasurable, <0.1 mg/cm^2 in 24 hours, but enough salt was deposited to induce accelerated attack in some of the test specimens. Samples with $CrCl_3 \cdot 6H_2O$-infiltrated coatings showed signs of accelerated attack after 24 hours, and by the end of five days, had lost 90% of their coating and were completely covered in corrosion product (Figure 42(c)). The uncoated alloy samples showed signs of accelerated attack after 48 hours, with the morphology of Type I hot corrosion observed near the edges. The micrographs in Figure 41 show the region of the uncoated sample where the attack changes from accelerated attack to normal oxidation. The dark regions on the left side of Figure 41(a) are internal oxides of aluminum and chromium. Beneath these oxides, internal attack of the alloy by sulfur was found, as evidenced by the dark grey particles of chromium-rich sulfide in Figure 41(b).

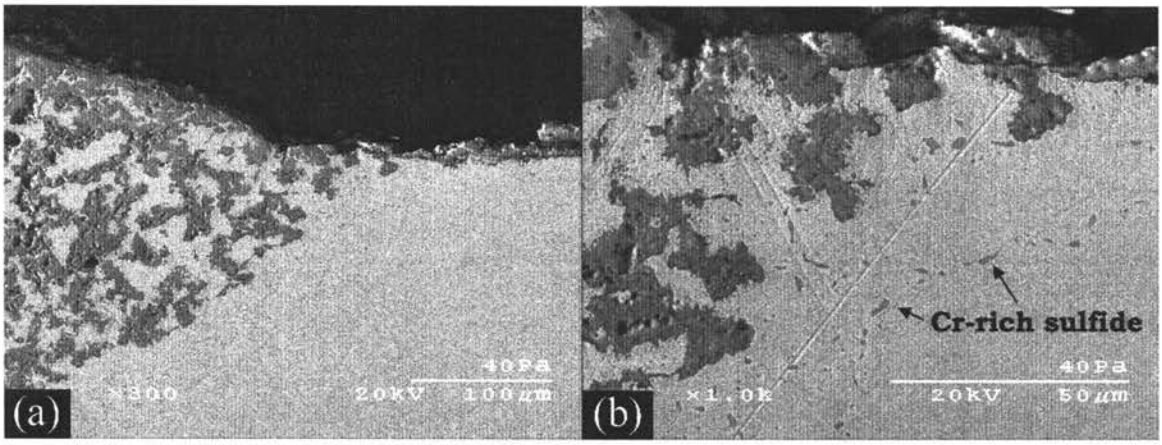

Figure 41. Bare substrate tested in Dean Rig at 900°C for 5 days, seen at (a) 300x and (b) 1000x.

Micrographs of the four coated test specimens are shown in Figure 42. The as-sprayed YSZ coated sample, Figure 42(a), showed some pitting of the substrate at the coating-substrate interface. The coating is still well adhered to the substrate, but the pitting of the substrate results in a smaller adherent surface area. The as-sprayed physical blend coating, Figure 42(b), appears much like the coating oxidized without salt, Figure 34(b). The $CrCl_3 \cdot 6H_2O$-infiltrated coating, Figure 42(c), fared the worst of all the APS coated coupons. The coating completely delaminated from the substrate, and Type I morphology is seen with the internal sulfides. In comparison, the $MgCrO_4 \cdot 5H_2O$-infiltrated coating fared very well. No internal sulfidation was observed, and the interface looks much like that seen in Figure 34(b).

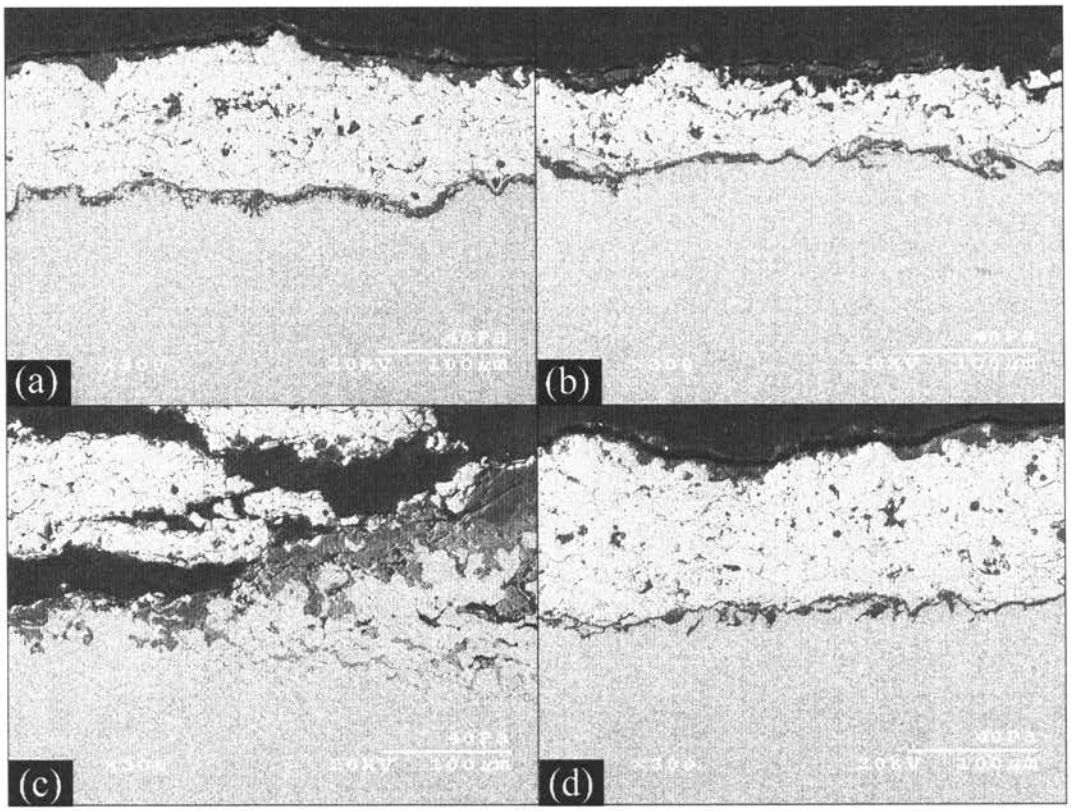

Figure 42. APS coatings tested 5 days in Dean Test with Na2SO4: (a) as-sprayed YSZ, (b) as-sprayed physical blend, (c) CrCl3·6H2O-infiltrated coating, and (d) MgCrO4·5H2O-infiltrated coating.

Additional Dean Rig tests with pre-deposited salt were subsequently carried out to be sure that enough salt was present to induce hot corrosion in the samples that appeared highly resistant. The specimens from these tests showed more attack than the previous Dean Rig tests, but showed no easily discernable difference in the hot corrosion resistance of any of the coatings. $CrCl_3$-infiltrated coatings were omitted from these and subsequent tests because of their obvious susceptibility to attack by molten salt. Micrographs of the three coatings subjected to a 48h "pre-deposit" test are shown in Figure 43.

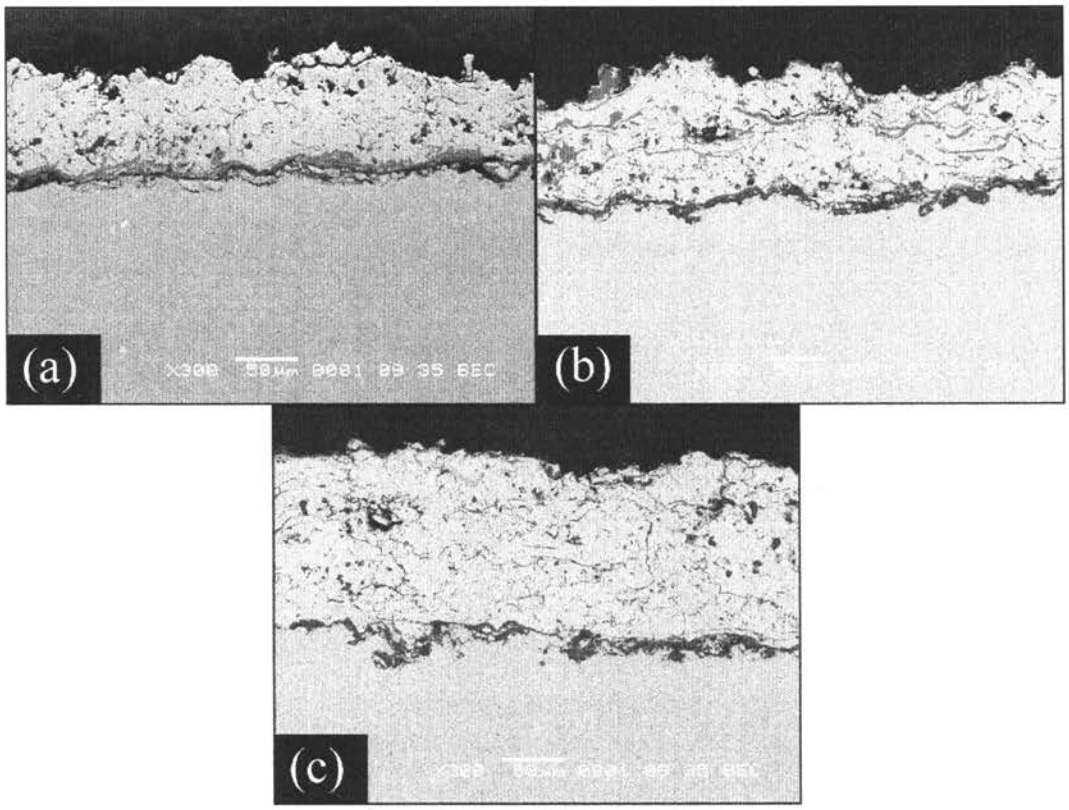

Figure 43. Samples from 48-hour Dean Rig test with pre-deposited Na_2SO_4 (a) as-sprayed YSZ, (b) physical blend, and (c) $MgCrO_4$-infiltrated coating.

This "pre-deposit" Dean Rig tests were carried out to ten days, and the samples showed a significant amount of accelerated attack, but the attack clearly began along the edges of the coating, so determination of an inferior or superior coating could not be accurately made.

5.3.4 Dean Rig Testing with Coatings from Modified Powders

Dean Rig tests were carried out using test specimens with the coatings described in section 4.1. Dean Rig testing of the spray-dried coatings produced sulfides in the alloy, a relatively thick layer of oxide (~10μm), and a crumbling coating, as seen in Figure 44(a). Samples with coatings from fused and crushed powders repeatedly lost their coatings, sometimes in as

little as 24 hours in the Dean Rig at 900°C. Coatings produced with infiltrated powders appeared to be crumbled after 48 hours in the Dean Rig at 900°C, Figure 44(b).

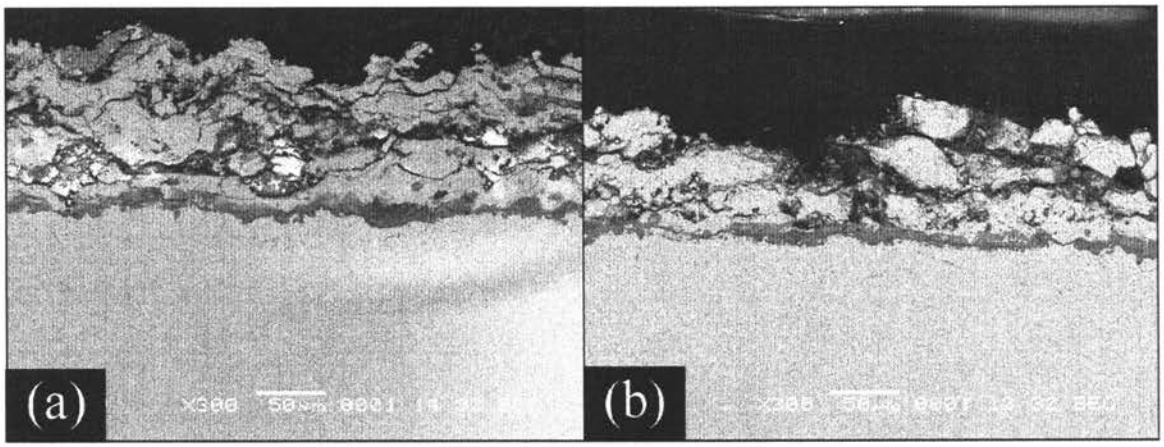

Figure 44. Coating produced (a) with spray-dried powders and (b) with infiltrated powders after 48 hours in Dean Rig at 900°C with pre-deposited Na_2SO_4 replenished after 24 hours.

The poor performance of these coatings is believed to be a result of the conditions used in the APS coating procedure. The modified coatings were sprayed with using the same parameters and conditions as the pure YSZ coatings, but the modified powders had different size distributions and different densities, which could have resulted in inferior coatings. The determination of optimum APS parameters for these powders is beyond the scope of this study, so investigation of coatings from modified powders was ceased.

5.3.5 Crucible Tests

The crucible test specimens employed in this study were designed to eliminate the edge effects seen in the Dean Rig and pre-deposited salt tests.

These tests were carried out with three different coatings (YSZ, physical blend, and $MgCrO_4$-infiltrated YSZ) on two different substrates (Haynes 214 and Ni 200).

5.3.5.1 Haynes 214 Substrate

Figure 45 shows representative micrographs of the coated Haynes 214 samples that were subjected to 4, 16, and 48-hour crucible tests in Na_2SO_4 at 900°C. The 48-hour samples show a degree of accelerated attack, which appeared to begin as a local attack, but eventually broadens to a relatively uniform front. This attack is manifested as a distribution of narrow, deep pits in the alloy. The $MgCrO_4$-infiltrated coating, Figure 45(c), appears to be in the beginning stages of this attack. There were regions of relatively deep attack as well as regions of clean interface. The YSZ coating, Figure 45(a), showed a higher density of accelerated attack, and the physical blend coating, Figure 45(c), exhibited a nearly uniform front of accelerated attack.

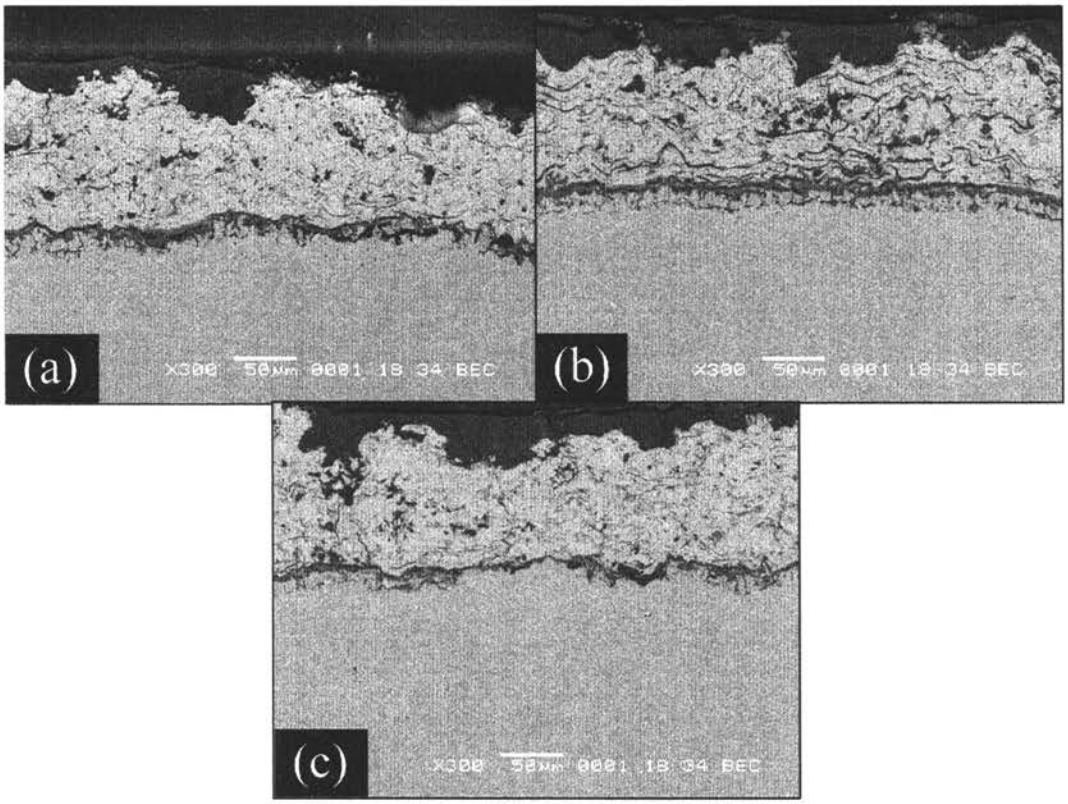

Figure 45. Samples from 48-hour crucible test with Na_2SO_4 on Haynes 214 substrate (a) as-sprayed YSZ, (b) physical blend, and (c) $MgCrO_4$-infiltrated YSZ.

Upon closer inspection of the physical blend coating, an interesting phenomenon was observed. It appeared that the salt had dissolved Cr_2O_3 out of the coating, in fact, some of the coatings had almost no Cr_2O_3 left in them. Figure 46 shows a Cr_2O_3 particle in the coating that has been partially dissolved by Na_2SO_4. This dissolution of Cr_2O_3 produces more pore space in the coating and a larger area for the salt to contact the substrate. This is believed to be at least part of the reason that the samples coated with physical blend showed such extensive attack. A fine distribution of Cr, like in the $MgCrO_4$-infiltrated coating, appears to have a beneficial effect on reducing or delaying the hot corrosion attack.

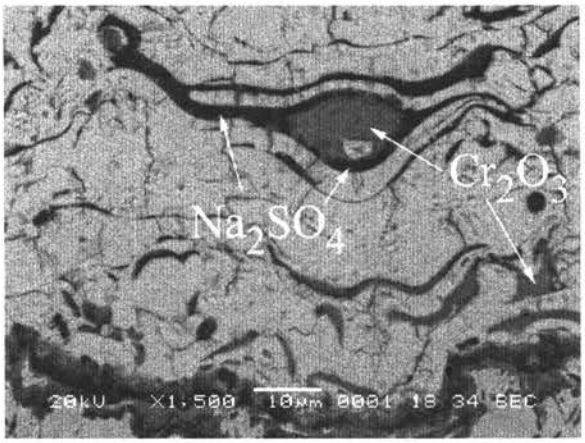

Figure 46. Micrograph showing evidence of Cr_2O_3 dissolution by Na_2SO_4.

The color of the Na_2SO_4 used in the crucible tests changed over the time of the 48-hour test. The salt turned yellow, the signature of CrO_4^{2-}, and was observed to be a more intense yellow for the physical blend and $MgCrO_4$-infiltrated samples than for untreated YSZ. The CrO_4^{2-} can come either from the coating or the alloy, and as the 4-hour crucible test samples showed very little attack of the substrate, it is believed that the vast majority of the yellow color came from the coating. These salts after a 4-hour crucible test are shown in Figure 47. The salt used for the YSZ coating appears white because there is no Cr in the coating and the substrate has not been attacked yet. The other two salts appeared bright yellow as Cr had been dissolved out of the coatings.

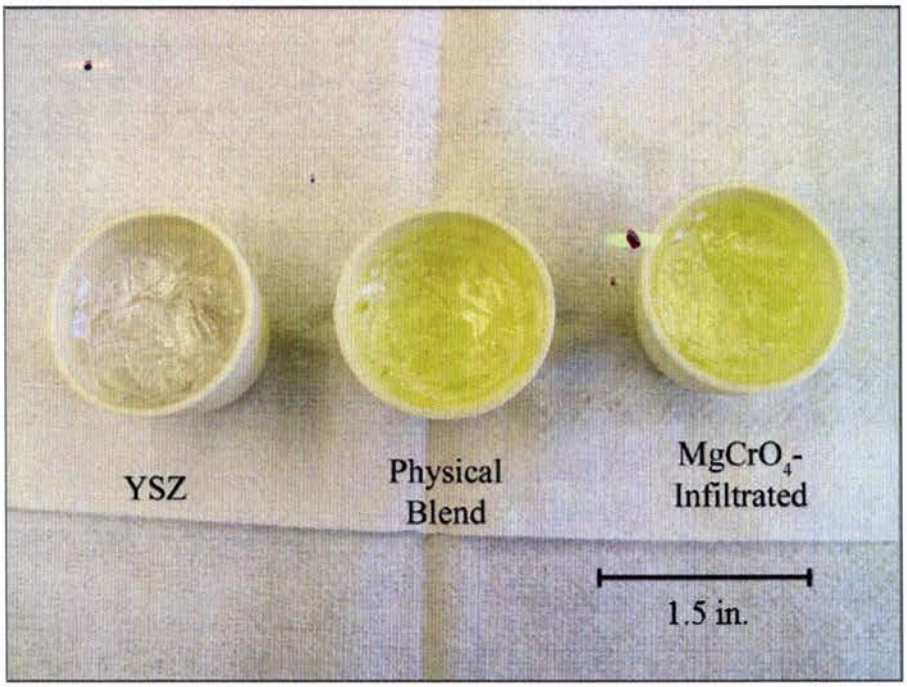

Figure 47. Crucibles of salt after 4-hour crucible test.

The extent of attack was quantified by measuring the depth of the massive attack, shown in Figure 17, of each sample. The results along with the standard deviation of each measurement are shown in Figure 48. The standard deviations are seen to overlap the data heavily, but a general trend can be seen, and is consistent with the results observed in Figure 45. The large standard deviation of the data can be explained by the fact that the attack is observed as a distribution of pits and that the measurement of the depth of these pits will invariably hit points where no pit is present.

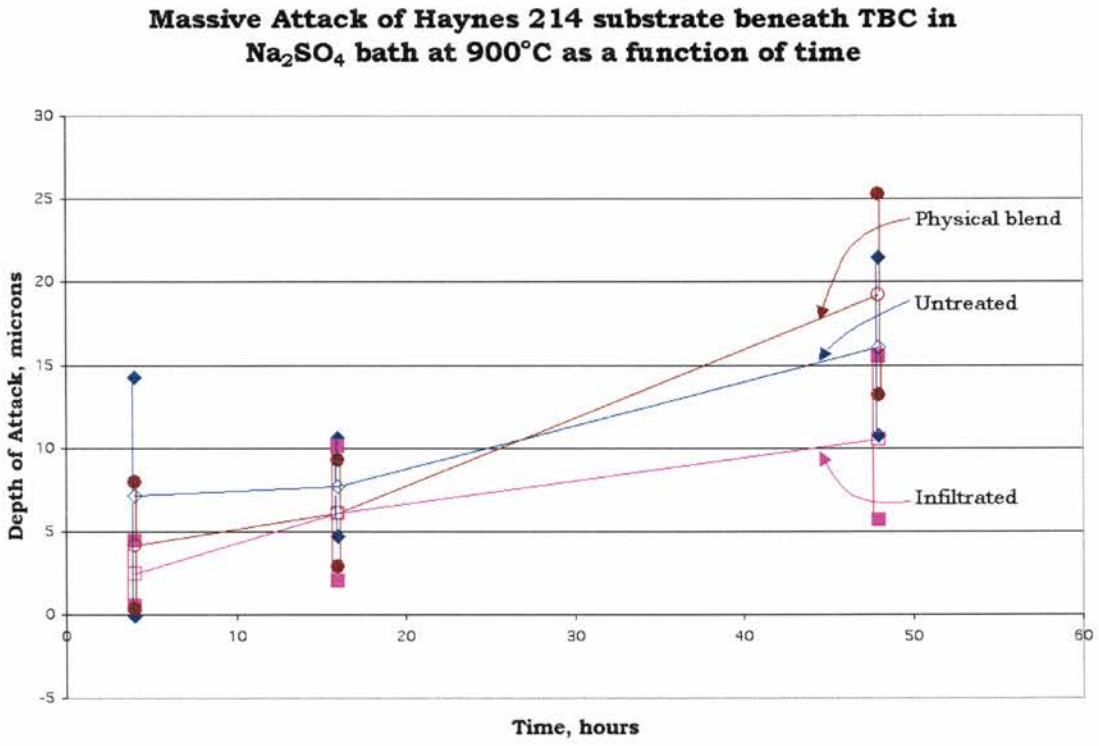

Figure 48. Plot of massive attack versus time for three coated sample types in Na_2SO_4 crucible test (Haynes 214 substrate).

As shown in Chapter 4, the pin samples were made with two thicknesses of coating. The massive attack of the substrate beneath the thick and thin coatings were measured and compared, Figure 49. These data show that the thickness of the coating had no statistically significant effect on the depth of massive attack of the underlying substrate.

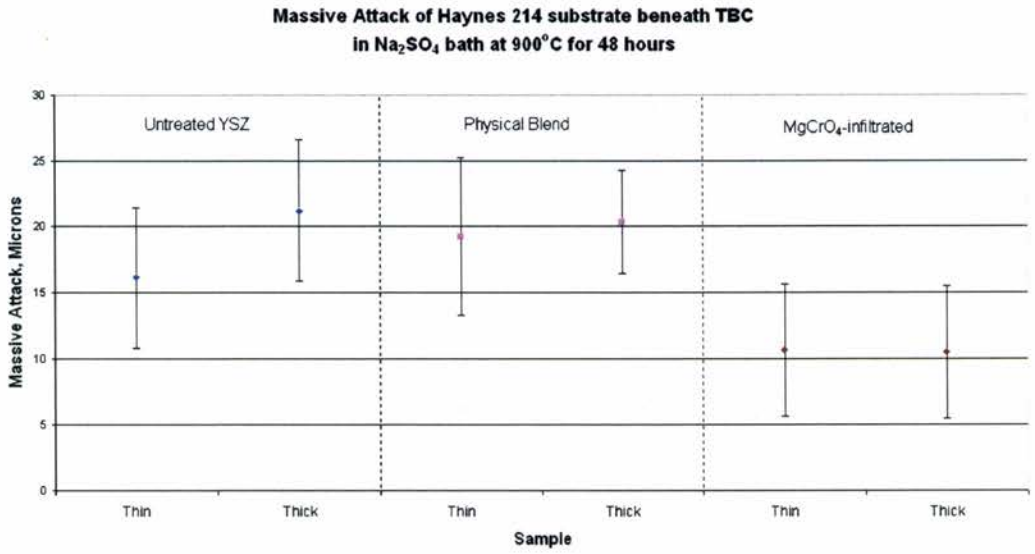

Figure 49. Comparison of massive attack depth between thin (~100µm) and thick (~300µm) coatings for Haynes 214 substrates in 48-hour crucible test. The error bars are ±1 standard deviation of all values measured at that point.

5.3.5.2 Nickel 200 Substrate

Crucible tests were also carried out on samples with Ni 200 substrates. The extent of attack on these samples was much greater than that seen with Haynes 214, and the morphology appeared different as well. A thick porous oxide grew between the coating and substrate, and nickel sulfides were found deep into the metal. It is recalled that nickel sulfide is liquid at 900°C and it could partially wet the grain boundaries of the metal. As shown in Figure 50, YSZ and the $MgCrO_4$-infiltrated YSZ appear to have experienced the same amount of attack, while the physical blend coated sample was attacked the most. As in the tests with Haynes 214, the physical blend coating lost most of its Cr_2O_3 due to dissolution in Na_2SO_4.

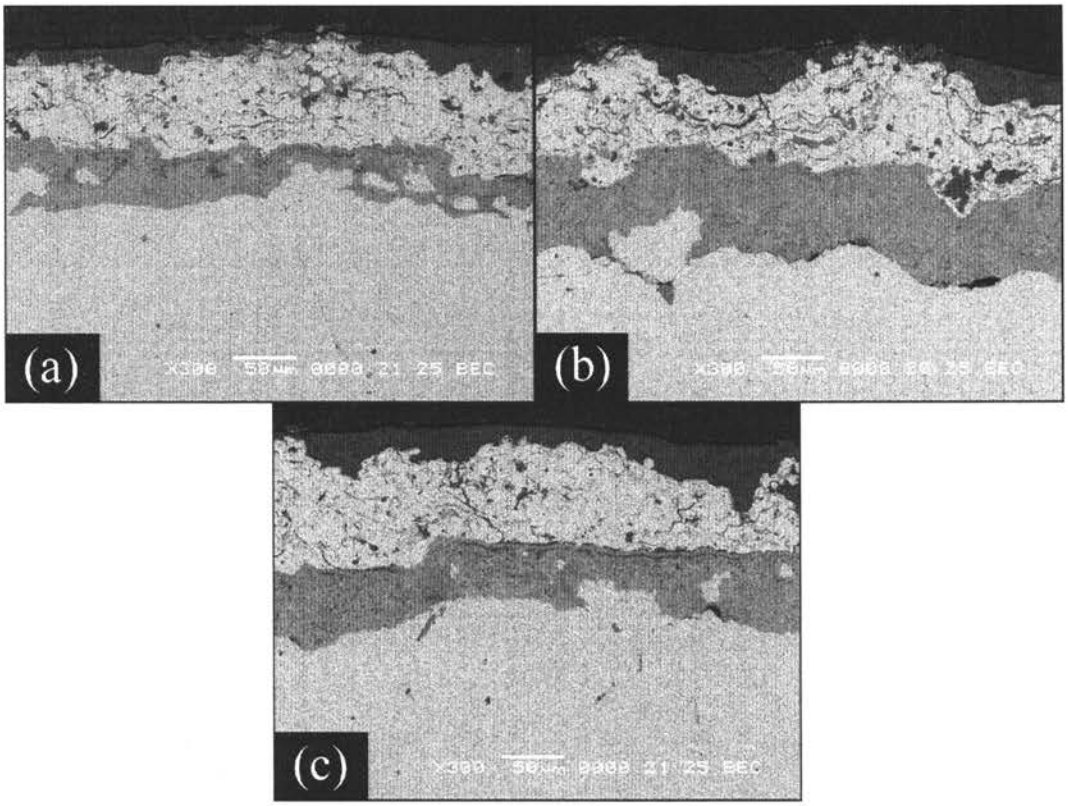

Figure 50. Samples from 10-hour crucible test with Na_2SO_4 on Ni 200 substrate (a) as-sprayed YSZ, (b) physical blend, and (c) $MgCrO_4$-infiltrated YSZ.

When the depth of attack was quantified for the coated Ni 200 samples, the trend still showed that the physical blend provided the least resistance to accelerated attack, but it was not possible to determine whether YSZ or $MgCrO_4$-infiltrated YSZ is better. These results are shown in Figure 51. In a comparison between Figures 48 and 51, it can be seen that the Ni 200 samples exhibited much deeper attack than the Haynes 214 samples, which is expected since the Al and Cr would act to improve the oxidation and corrosion resistance of the 214 alloy.

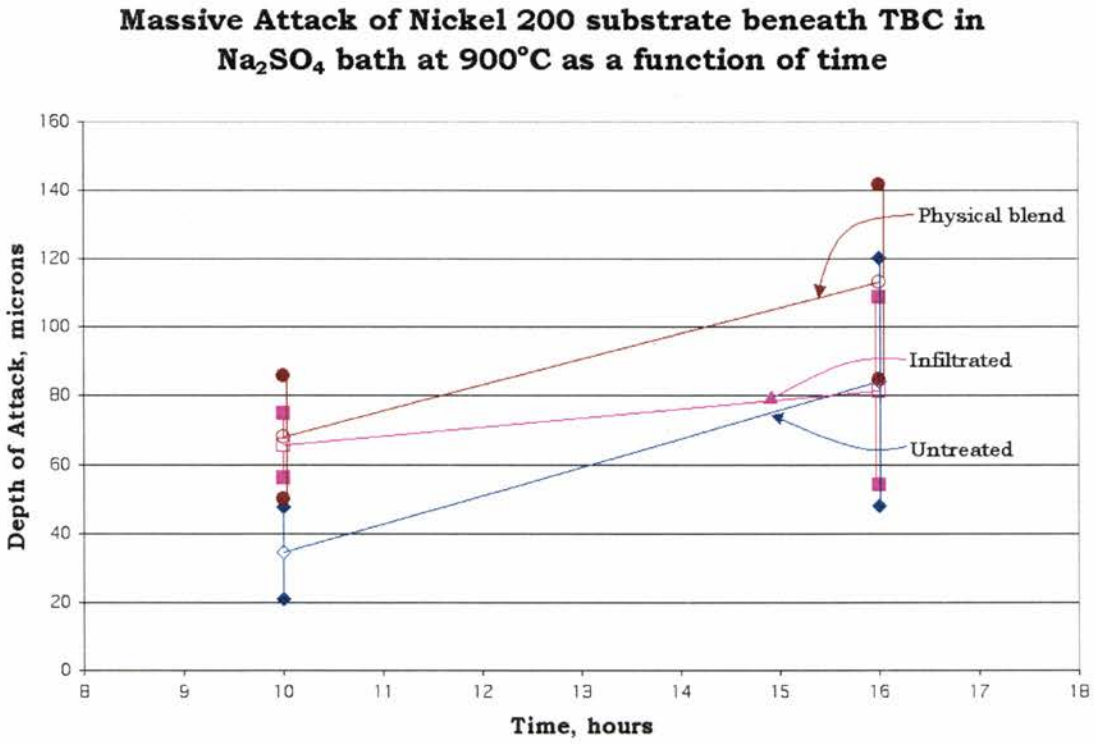

Figure 51. Plot of massive attack versus time for three coated sample types in Na2SO4 crucible test (Ni 200 substrate).

The effect of top-coat thickness was also investigated with Ni 200 substrates, and the results are shown in Figure 52. As with the Haynes 214 samples, coating thickness had no apparent significant effect on the depth of massive attack.

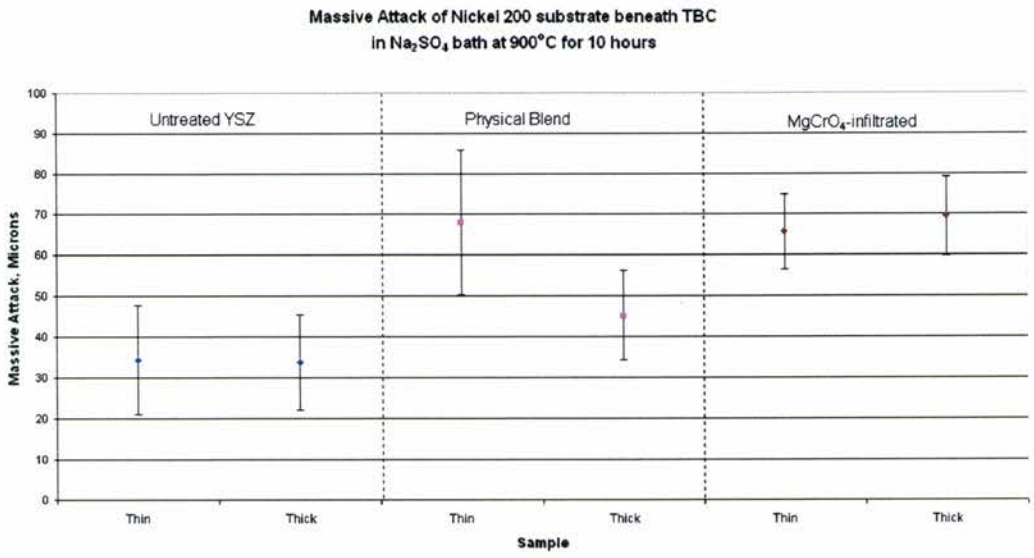

Figure 52. Comparison of massive attack depth between thin (~100µm) and thick (~300µm) coatings for Nickel 200 substrates in 10-hour crucible test. The error bars are ±1 standard deviation of all values measured at that point.

5.5.3.3 Cyclic Crucible Tests

A cyclic hot corrosion crucible test was performed in an attempt to assess the tendency of the coating to crack due to differential volume changes of the salt in the coating during cooling from the reaction temperature. In parallel, a cyclic oxidation test in the absence of salt was carried out as a comparison. The oxidation test was carried out for 10 cycles, each of which consists of 1 hour at temperature (900°C) followed by cooling in room temperature air for approximately 10 minutes. The coatings changed color slightly from their original state, and the uncoated portion of the samples appeared to show some light oxidation, but macroscopically, the samples, as seen in Figure showed no coating damage.

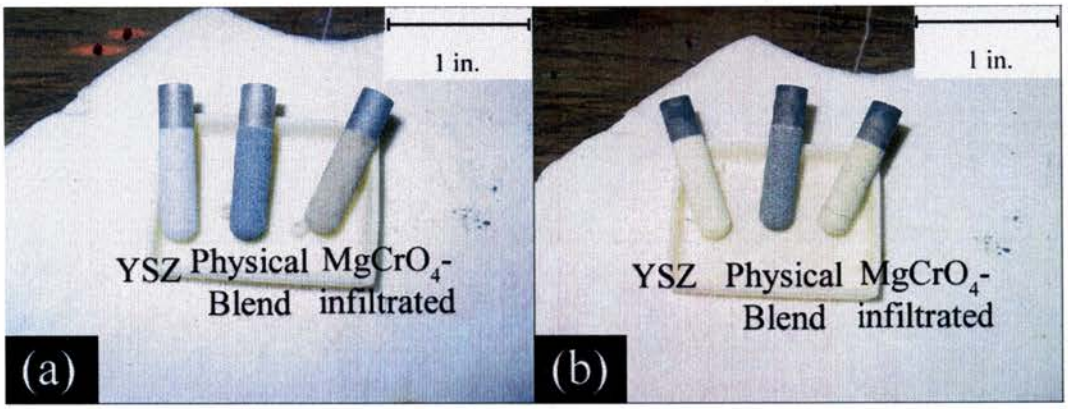

Figure 53. Cyclic oxidation samples (a) before oxidation and (b) after 10 1-hour cycles at 900°C in air.

These oxidized samples had virtually unchanged microstructure in the coating bulk, but each showed areas of delamination along the TGO/top-coat interface. Figure 54 shows the coatings and the substrate/TGO/top-coat interface regions of the cyclic oxidation samples. Areas of delamination of the coating from the thermally grown oxide are indicated with arrows in the inlay micrographs. This delamination behavior clearly comes from the temperature cycles as it was not observed in an isothermally oxidized sample, as seen in Figure 34(b).

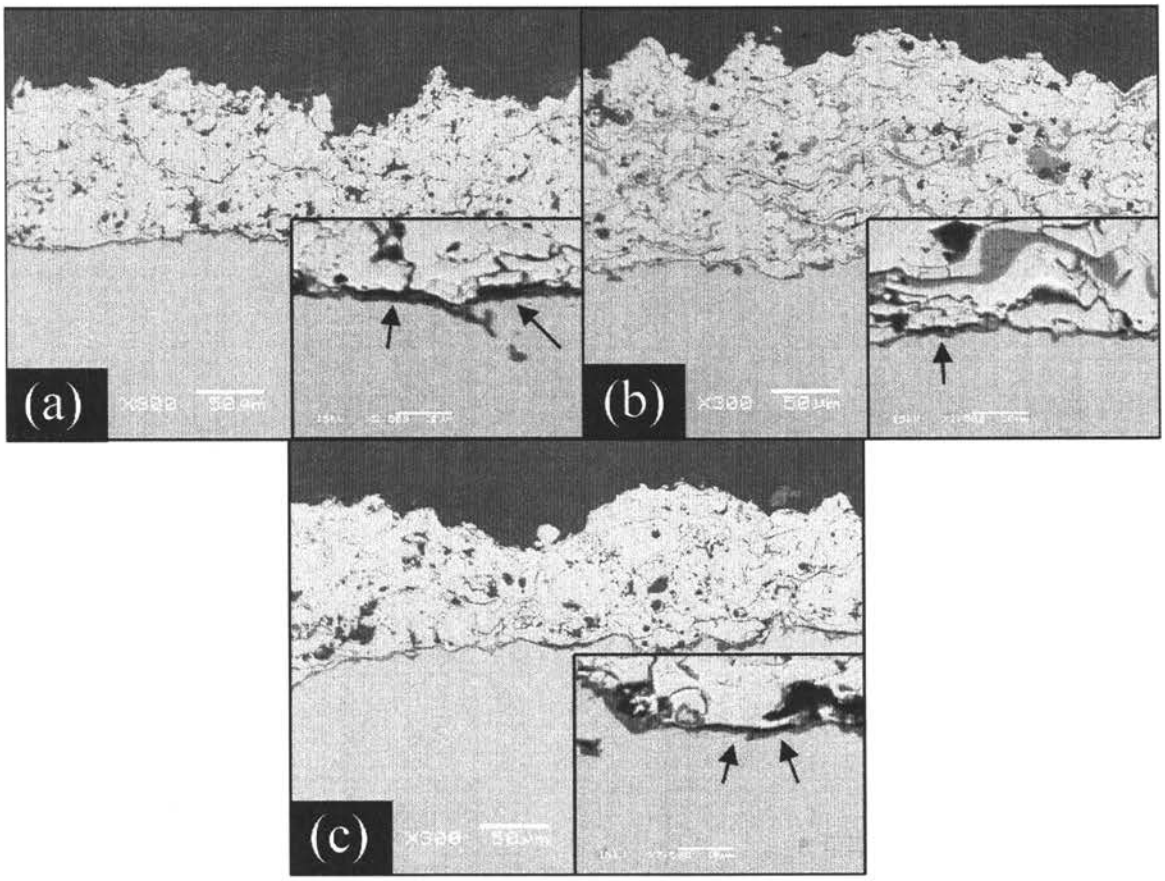

Figure 54. Micrographs of (a) untreated YSZ, (b) physical blend, and (c) $MgCrO_4$-infiltrated cyclic oxidation samples (10 1-hour cycles at 900°C). Inlays show high magnification image of interface with regions of delamination indicated.

The cyclic crucible test was carried out for 10 1-hour cycles, after which the coatings began to fall off. Figure 55 shows the specimens before testing and after 10 1-hour cycles. A large crack can be seen in the thick portion of the YSZ coating, which was almost completely separated from the substrate.

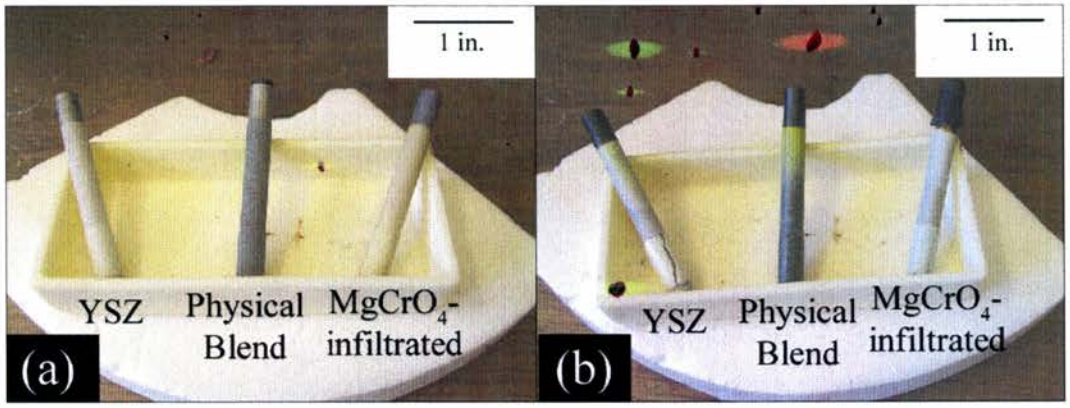

Figure 55. Cyclic crucible test specimens (a) before testing and (b) after 10 1-hour cycles.

These samples were observed in an SEM after testing, and it was seen that the thick coatings were completely delaminated, severely cracked and salt had come in direct contact with the alloy, as seen in Figure 56. However, very little accelerated attack was observed. The complete failure of the thick coating could be due to the increased internal stresses that arise from the APS deposition of a thicker coating(37), from the volume difference effects of cycling temperature when the pores of the coating are filled with salt or from a combination of both.

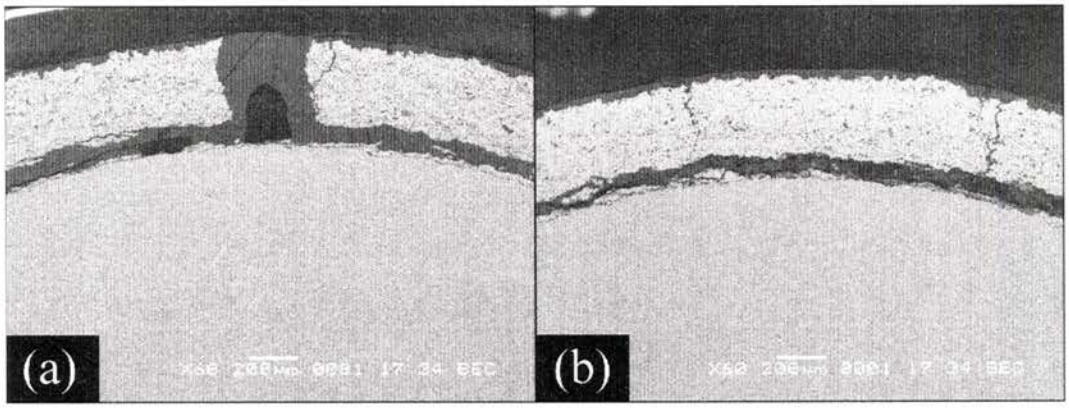

Figure 56. Thick coating from (a) physical blend and (b) $MgCrO_4$-infiltrated samples after 10 1-hour crucible test cycles.

The thin coatings, seen in Figure 57, remained intact with a slight increase in the amount of vertical cracking in the coating. The coatings appeared well adhered and the interfaces relatively clean. Small localized areas of accelerated attack were observed, as evidenced in Figure 58. The lack of catastrophic accelerated attack is understandable as the samples were only in the presence of the salt for 10 hours, and, as was discussed in Section 3.4.4, uncoated Haynes 214 lasted 12 hours in the presence of a thin salt film before accelerated attack observed. With the coating still intact, catastrophic accelerated attack would not be expected until well beyond 10 hours. No noticeable difference was present in the interfacial appearance of any of these thin-coated samples.

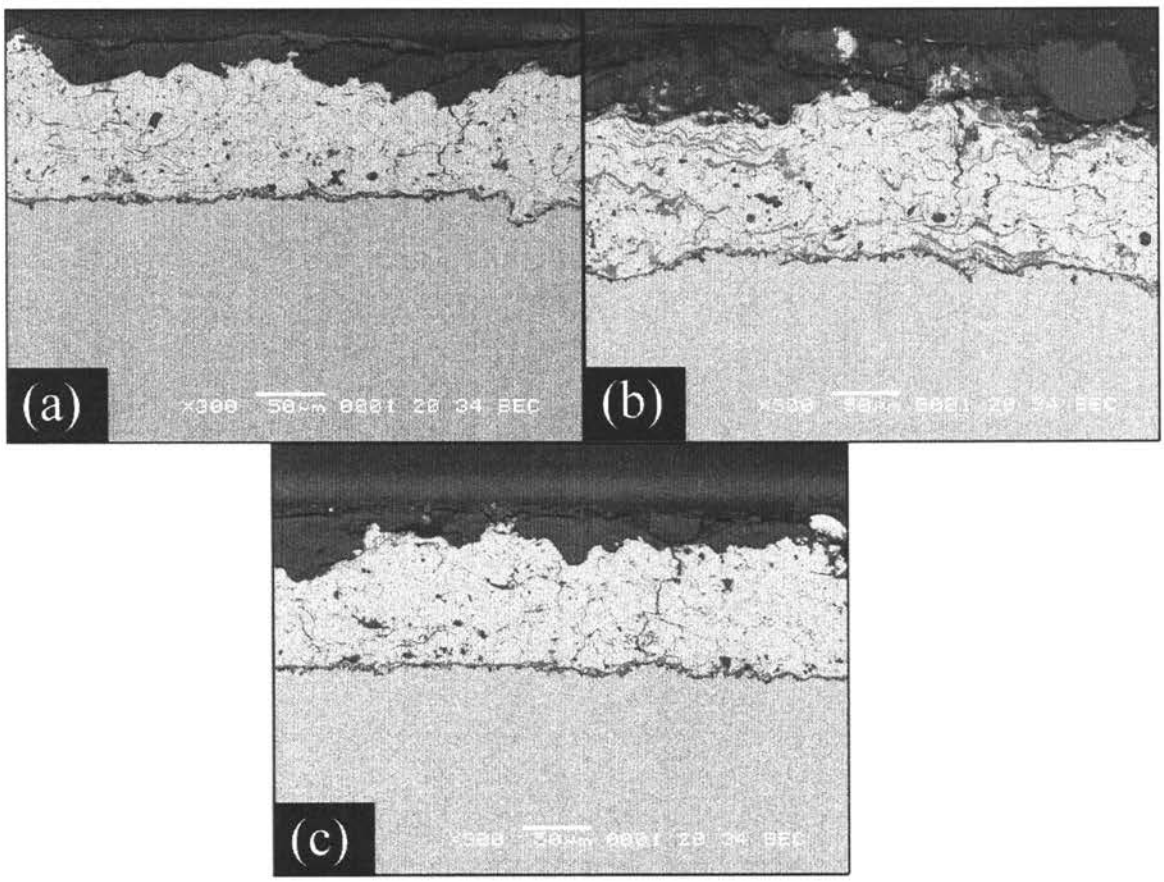

Figure 57. Thin coatings from (a) YSZ, (b) physical blend, and (c) $MgCrO_4$-infiltrated samples after 10 1-hour crucible test cycles.

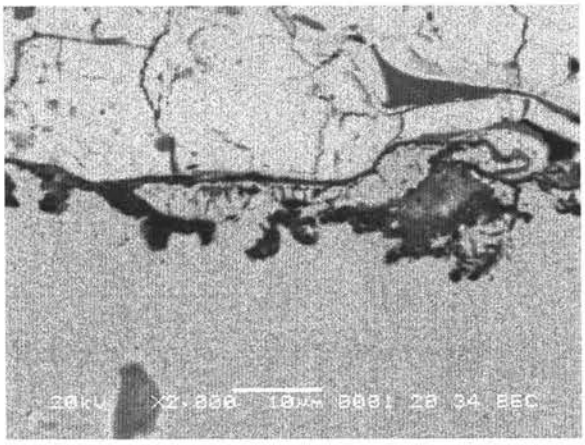

Figure 58. Micrograph of cyclic crucible test sample with thin physical blend coating showing beginnings of accelerated attack.

Thermal cycling of a TBC system caused coating and interface damage in excess of that observed in isothermal experiments. In the presence of salt, the differential volume changes upon heating and cooling created cracks in the coating which decreased the mechanical stability of the coating and provided more paths for the salt to access the alloy. In the absence of salt, 10 thermal cycles caused minor delaminations of the coating which could lead to spallation of the coating upon additional thermal cycles.

Chapter 6: Summary

The hot corrosion resistance of gas turbine engines has been and continues to be a major concern in the field of high temperature corrosion. The vast majority of work in the area of hot corrosion resistance has been focused on the development of resistant alloys and bond-coats (in TBC systems). It has long been known that Cr is a beneficial alloying addition for hot corrosion resistance, and that the salts observed in gas turbine engines contain several, primarily sulfate, components. This previous knowledge has been used in the present study to develop a new way to increase the hot corrosion resistance of a TBC system. This study has examined the use of the top-coat as a carrier of elements (Mg and Cr) that, when dissolved, reduce the ability of a salt to cause accelerated attack of a metal.

The methods investigated for the modification of the top-coat included infiltration with water-soluble, Cr- and Mg- containing compounds and APS coating with Cr-containing powders. It was shown that these modification methods produced coatings with measurable amounts of modifying oxides while maintaining approximately the same microstructure and crystal structure of the YSZ.

The next step was to test the resistance of these top-coat systems to hot corrosion in the presence of liquid salt. The selection and development of a test that produced accelerated attack of the coating by salt access through the coating in a reasonable amount of time proved to be a challenging task. Pre-deposited salt tests, Dean Rig tests, and crucible tests were performed. The Dean Rig produced atmospheric conditions nearest to those in a gas turbine engine and mitigated the problem of decomposition of the Na_2SO_4-

$CaSO_4$-$MgSO_4$ ternary salt, but the crucible test, as described in Section 3.2.2, proved to be the most effective way to get hot corrosion in coated samples without observing the effects of coating edges.

The crucible tests showed that the $MgCrO_4$-infiltrated samples were more resistant to hot corrosion than untreated YSZ samples. The physical blend exhibited less resistance to hot corrosion than the untreated YSZ samples. In fact, during longer tests (48 hours) the physical blend samples showed almost complete dissolution of the coarsely dispersed Cr_2O_3, resulting in more area of contact between salt and metal. The idea that a fine distribution of modifying oxides is better was illustrated by the improved resistance of $MgCrO_4$-infiltrated samples. It is important to note that the hot corrosion resistance of the $MgCrO_4$-infiltrated coatings was not dramatically better than that of the other coatings. Every type of coating exhibited signs of accelerated attack under the limited set of hot corrosion testing conditions examined in this study.

The inclusion of Cr in either the salt or the coating will *delay* the onset of hot corrosion in modern TBC systems, but it *will not prevent* this type of attack. It is believed that the best way to improve the hot corrosion resistance of a TBC system is to produce a highly resistant bond-coat or substrate. A top-coat modified with a fine distribution of Cr or Cr and an AE metal could be included as an added measure of protection. Of the methods considered in this study, the simplest and most effective way to create this fine dispersion of Cr and AE metal is by the infiltration of YSZ coatings with solutions of Cr- and AE- containing oxide precursors.

Chapter 7: Future Work

The work presented in this thesis has shown that the top-coat modifications applied here have the ability to slightly increase the hot corrosion resistance of a top-coat/substrate system, but that the underlying alloy has a much greater bearing on the resistance of the system. For this reason, it is recommended that future work consider the variation of the substrate material (*e.g.*, actual bond coat compositions) in addition to further investigation of top-coat modification. Further investigation of top-coat modifications could include attempts to make high-quality coatings from the modified coatings discussed in Section 4.1.2 or modifications with Ca individually or in addition to Mg and/or Cr in order to change the composition of a multi component (possibly eutectic) salt

Several effective experimental techniques have been established, and could be used in the investigation of top-coated samples with various bond-coat substrates. In addition to the experimental methods set forward in this thesis, the investigation of top-coated samples by electrochemical methods appears to be an interesting technique and could be used to determine corrosion rates, corrosion potentials, and accelerated attack breakaway points. This could give a better understanding of how a coating modification increases the resistance of a TBC system.

References

1. Stringer J. 1987. *Materials Science and Technology* 3: 482-93
2. Driver D, Hall DW, Meetham GW. 1981. In *The development of gas turbine materials*, pp. 1-30. London: Applied Science Publishers, Ltd.
3. Davis JR, ed. 2000. *ASM Specialty Handbook: Nickel, Cobalt, and Their Alloys*. Materials Park, OH: ASM International. 425 pp.
4. Hancock P. 1987. *Materials Science and Engineering* 88: 303-11
5. Haynes 214 alloy Principle Features. http://www.haynesintl.com/214H3008C/214pf.htm (date accessed: 16 April 2003). 2003, Haynes© International.
6. Goebel JA, Petit FS. 1970. *Metallurgical Transactions* 1: 1943-54
7. Otsuka N, Rapp RA. 1990. *Journal of the Electrochemical Society* 137: 53-60
8. Otsuka N, Rapp RA. 1990. *Journal of the Electrochemical Society* 137: 46-52
9. Wu YM, Rapp RA. 1991. *Journal of the Electrochemical Society* 138: 2683-90
10. Hasselman DPH, Johnson LF, Bentsen LD, Syed R, Lee HL, Swain MV. 1987. *American Ceramic Society Bulletin* 66: 799-806
11. Padture NP, Gell M, Jordan EH. 2002. *Science* 296: 280-4
12. Herman H. 1988. *Scientific American* 256: 112-7
13. Shores DA. 1983. In *High temperaure corrosion : March 2-6, 1981, San Diego, California*, ed. RA Rapp, pp. 493-501. Houston, Texas: National Association of Corrosion Engineers
14. Decrescente MA, Bornstein NS. 1968. *Corrosion* 24: 127-33
15. Bornstein NS. 1996. *JOM* 48: 37-9
16. Simons EL, Browning GV, Liebhafsky HA. 1955. *Corrosion* 11: 505-14
17. American Ceramic Society., Materials Science and Engineering Laboratory (U.S.). Ceramics Division. 1992. Phase equilibria diagrams. pp. v. Westerville, Ohio: American Ceramic Society
18. Goebel JA, Petit FS, Goward GW. 1973. *Metallurgical Transactions* 4: 261-78
19. Zhang YS. 1986. *Journal of the Electrochemical Society* 133: 655-7
20. Zhang YS, Rapp RA. 1985. *Journal of the Electrochemical Society* 132: 734-5
21. Rapp RA. 1986. *Corrosion* 42: 568-77
22. Jose PD, Gupta DK, Rapp RA. 1985. *Journal of the Electrochemical Society* 132: 735-7
23. Rapp RA, Goto KS. 1981. In *Proceedings of the Second International Symposium on Molten Salts*, ed. J Braunstein, JR Selman, pp. 159-73. Pennington, NJ: The Electrochemical Society
24. Rapp RA. 2002. *Corrosion Science* 44: 209-21
25. Lowell CE, Deadmore DL. 1978. *Corrosion Science* 18: 747-63

26. Smeggil JG. 1999. In *Elevated Temperature Coatings: Science and Technology III*, ed. JM Hampikian, NB Dahotre. Warrendale, Penn.: Minerals Metals & Materials Society
27. Akinc M, Sordelet DJ. 1987. *Advanced Ceramic Materials* 2: 232-8
28. Akinc M, Sordelet DJ, Munson M. 1988. *Advanced Ceramic Materials* 3: 211-6
29. Sordelet DJ, Akinc M. 1988. *Journal of Colloid and Interface Science* 122: 47-59
30. Sordelet DJ, Akinc M, Panchula ML, Han Y, Han MH. 1994. *Journal of the European Ceramic Society* 14: 123-30
31. Steinmetz P, Duret C, Morbioli R. 1986. *Materials Science and Technology* 2: 262-71
32. Saunders SRJ, Nicholls JR. 1984. *Thin Solid Films* 119: 247-69
33. Swindells N, Raper K, Stewart M. 1983. *High Temperature Technology* 2: 139-45
34. Bornstein NS, Allen WP. 1997. *Materials Science Forum* 251-254: 127-34
35. Hancock P. 1987. *Materials Science and Technology* 3: 536-44
36. Lai GY. 1990. *High-Temperature Corrosion of Engineering Alloys.* Materials Park, OH: ASM International. 231 pp.
37. Smart RF, Catherall JA. 1972. *Plasma Spraying.* London,: Mills and Boon